Received: 20 February 2023 | Revised: 20 February 2024 | Accepted: 10 March 2024

DOI: 10.1111/jmg.12772

Journal of METAMORPHIC GEOLOGY WILEY

ORIGINAL ARTICLE

Metasomatism of the continental crust and its impact on surface uplift: Insights from reactive-transport modelling

James R. Worthington[1] | **Emily J. Chin**[1] | **Richard M. Palin**[2]

[1]Scripps Institution of Oceanography, University of California San Diego, La Jolla, California, USA

[2]Department of Earth Sciences, University of Oxford, Oxford, UK

Correspondence
James R. Worthington, Scripps Institution of Oceanography, University of California San Diego, La Jolla, CA, USA.
Email: jworthin@ucsd.edu

Funding information
United States National Science Foundation, Division of Earth Sciences, Tectonics and Petrology and Geochemistry programs, grant # EAR-1926134.

Handling Editor: Dr. Katy Evans

Abstract

High-elevation, low-relief continental plateaus are major topographic features and profoundly influence atmospheric circulation, sediment transport and storage, and biodiversity. Although orogenic surface-uplift mechanisms for modern continental plateaus near known plate margins like Tibet are well-characterized, they cannot account for examples in intracontinental settings like the Colorado Plateau. In contrast to canonical plate-tectonic uplift mechanisms, broad-scale hydration-induced metasomatism of the lower crust has been suggested to reduce its density and increase its buoyancy sufficiently to contribute to isostatic uplift. However, the relationships between key petrophysical properties in these environments are not fully quantified, which limits application of this model. Here, we develop a series of petrological models that describe the petrological and topographic effects of fluid–rock interaction in non-deforming continental crust of varying composition. We apply an open-system petrological modelling framework that utilizes reactive-transport calculations to determine the spatial and temporal scales over which mineralogic transformations take place compared with the magnitude of infiltration of aqueous fluids derived from devolatilization of subducting oceanic lithosphere. The buoyancy effect of hydration-induced de-densification is most significant for metabasic lower crust, intermediate for metapelitic crust, and minimal for granodioritic crust. We apply these results to a case study of the ~2 km-high Colorado Plateau and demonstrate that under ideal conditions, hydration of its lower–middle crust by infiltrating aqueous fluids released by the Farallon slab during Cenozoic low-angle subduction could have uplifted the plateau surface by a maximum of ~1 km over 16 Myr. However, realistically, although hydration likely has a measurable effect on surface tectonics, the uplift of orogenic plateaus is likely dominantly controlled by other factors, such as lithospheric delamination.

KEYWORDS
crustal hydration, metasomatism, petrological modelling, plateau uplift

---

1 | INTRODUCTION

The formation of intraplate continental plateaus is a longstanding geologic enigma. Classical plate tectonics predicts deformation concentrated at plate boundaries, but intraplate uplifts are characterized by diffuse lithospheric deformation far from plate boundaries (McKenzie & Parker, 1967; Molnar, 1988). Proposed mechanisms for driving surface uplift in intraplate settings commonly involve syn-rifting block uplift and rotation, mantle plume impingement, and delamination or thermal expansion of the lithosphere (Braun & Beaumont, 1989; Ebinger et al., 1989; Wichura et al., 2011). However, an understudied factor that can affect isostatic equilibrium is mineralogical changes driven by metasomatic alteration by aqueous fluids, which reduces the density of mid- to deep-crustal rocks via in situ metamorphic reaction (Guiraud et al., 2001).

Fluid–rock interactions occur widely throughout the continental crust, but the origins and mechanisms of such interactions are often poorly constrained (Yardley & Bodnar, 2014). Some general examples of deep crustal fluid–rock interactions include liberation of H_2O- and CO_2-rich fluids during prograde metamorphism resulting from sediment burial during orogenesis, crystallization, and subsequent enrichment in volatiles of magmas in the crust that stall during ascent towards the surface, or by devolatilization of subducted oceanic slabs (Figure 1a) (Etheridge et al., 1983; Hanson, 1992; Kerrick & Connolly, 2001; Peacock, 1990; Sun et al., 2004; Westrich et al., 1988). Petrological investigation of these metasomatic interactions is essential to quantify their potential to induce surface uplift in isostatically balanced continental crust, particularly as functions of temperature (T), pressure (P), and pre- and/or post-hydration bulk-rock composition (X).

In this study, we investigate the potential for subduction-devolatilization-related aqueous metasomatism of lower–middle continental crust to uplift plateaus far from plate boundaries. We model the implications of various hydration scenarios infiltrating a continental crustal column from its Moho (Figure 1b), specifically focusing on the time-resolved surface tectonic effects (i.e., change in elevation) of metamorphic de-densification by using novel reactive-transport petrological modelling. We use the ~2 km-high, $\sim 3.4 \times 10^5$ km^2 Colorado Plateau (USA) as a case study, as it is among Earth's most prominent intraplate uplifts and its position overlying the low-angle-subducting, dehydrating Farallon oceanic plate during the Cretaceous–Cenozoic enables the use of subduction-zone models to estimate fluid infiltration into its deep crust (Figure 1a) (Abers et al., 2020; Atwater, 1970; Condie, 1982; Hernández-Uribe & Palin, 2019b; Humphreys et al., 2003; Levander et al., 2011; Sahagian, 1987; Syracuse et al., 2010; van Keken et al., 2011). Although previous workers have laid the groundwork for quantifying the spatio-temporal relationships between hydration-driven density change and bulk-rock composition of the Colorado Plateau lower crust, the mass of aqueous fluid needed to produce measurable surface uplift has not been quantified or considered in terms of what subducting slabs can supply (Butcher et al., 2017; Levandowski et al., 2018; Porter et al., 2017). We demonstrate that a maximum of ~1.0 km of the surface uplift of the Colorado Plateau can potentially be attributed to hydration of its lower–middle crust by aqueous fluids derived from devolatilization of subducting Farallon oceanic lithosphere during the Cretaceous–Cenozoic. However, this maximum buoyancy estimate presumes 100%-efficient metasomatism of mostly metabasic lower crust, such that the effect is significantly reduced if fluid flow is channelized and bypasses some or all of the lower crust. Continued research into the grain-scale processes that allow fluid to percolate through high-grade metamorphic rocks will allow significant new advances to be made.

2 | GEOLOGICAL SETTING AND UPLIFT HISTORY OF THE COLORADO PLATEAU

The Colorado Plateau is one of Earth's most prominent geological structures, and its tectonic evolution has been intensely debated for over a century. The plateau is a broad region (~337,000 km^2) of high mean elevation (~2000 m above sea level) located in the southwestern interior of the USA (Figure 2). It comprises non-metamorphosed, non-deformed Paleozoic to Cenozoic sedimentary rocks overlying high-grade metamorphic Proterozoic basement (1.8–1.4 Ga) (Condie, 1982). It is bordered to the northwest by the Basin and Range province, to the northeast by the Rocky Mountains, and to the southeast by the Rio Grande Rift, all of which experienced significant Cenozoic orogenic activity and extensional tectonics (Flowers, 2010). The Great Plains to the east share a similar Mesozoic geological history to the plateau and overlie the same Proterozoic basement but are non-deformed (Whitmeyer & Karlstrom, 2007).

Late Cretaceous marine strata demonstrate that the region was below sea level at ~80 Ma, and various stages of tectonic uplift have been documented by multidisciplinary investigation, almost all of which are closely related to subduction of the Farallon oceanic plate beneath the southwestern USA since ~100 Ma (Atwater, 1970; Levander et al., 2011; Sahagian, 1987).

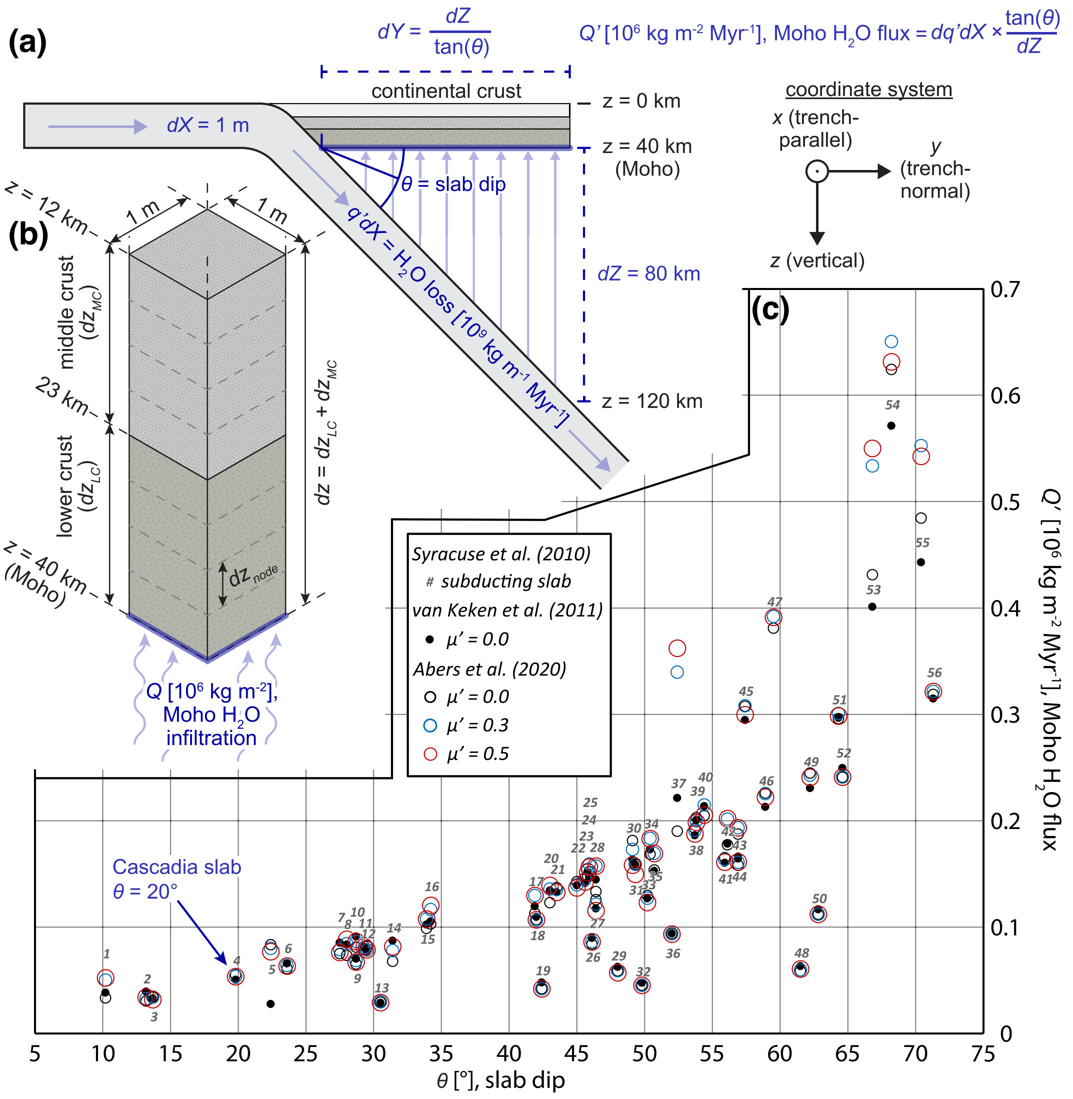

FIGURE 1 Tectonic–petrological model setup conditions. (a) Schematic cross section through a convergent margin showing parameters used to model dewatering of a subducting oceanic slab and release of H_2O into overlying lower crust. Assimilation of fluids into the mantle wedge is neglected in this scenario. (b) Schematic diagram showing model setup for reactive-transport calculations. See Appendix C for definition and explanation of individual parameters. (c) Estimated H_2O flux from 40–120 km-deep subducting slab into average overlying 1 m^2 Moho surface for 56 modelled subduction zones (Syracuse et al., 2010), ordered by slab-dip angle (Appendix A, Dataset S1). μ' is the effective friction coefficient and is used to model the effect of shear heating on the temperature of the subducting slab, which is most significant at <80 km depth (Abers et al., 2020).

Notably, the dip angle of the subducting slab is thought to have progressively flattened over time and exhibited a geodynamic configuration during much of the Cenozoic similar to the modern-day Pampean flat slab beneath the central Andes (Behr & Smith, 2016; Bird, 1988; Coney & Reynolds, 1977; Liu et al., 2010; Ramos et al., 2002; Ramos & Folguera, 2009). Various lines of evidence for a secular change in dip angle have been proposed, including delamination of mantle lithosphere and underplating of schists derived from the accretionary wedge beneath the volcanic arc, and cessation of arc magmatism and the progressive eastward migration of the magmatic front (Dickinson et al., 1978; Grove et al., 2003). Indeed, Oligocene–Miocene volcanic edifices (diatremes, plugs, and dikes) in the Four Corners region at the centre of the Colorado Plateau, ∼1000 km from the nearest tectonic plate boundary, contain a wide variety of mafic and ultramafic xenoliths that were metamorphosed and recrystallized from 80–30 Ma, potentially due to devolatilization of the Farallon slab and fluid release into the overlying lithospheric mantle wedge (Helmstaedt & Schulze, 1991; Smith, 2010; Usui et al., 2003). One of the effects of this putative flat slab beneath the plateau was widespread hydration of the mantle lithosphere (Li et al., 2008).

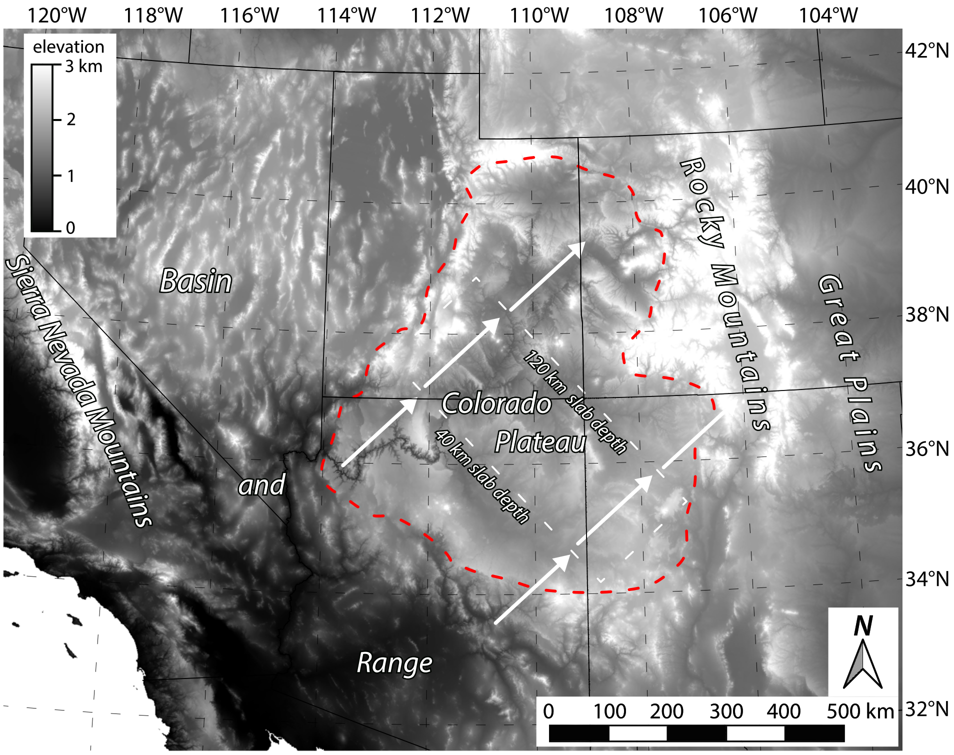

FIGURE 2 Map of the Colorado Plateau (outlined in red) and surrounding region. White-dashed, rectangular region schematically illustrates the scale, with respect to the Colorado Plateau, for a 220 km-long region of hydrated crust overlying the 20°-dipping, NE-subducting Farallon oceanic slab (white arrows) that corresponds to release of aqueous fluids between 40 and 120 km depth in our model setup. The precise location of the rectangular region of hydrated crust within the Colorado Plateau is arbitrary, may have migrated towards or away from the trench, and would have been longer or shorter for gentler or steeper dip angles throughout the life cycle of the subducting Farallon slab. Although the geometry of the Colorado Plateau was probably similar when the Farallon plate subducted beneath it during the late Cretaceous to early Cenozoic, the Basin and Range province was significantly less extensive from east to west.

However, it is not known to what extent such hydration extended into and/or affected the middle and/or deep crust of the (proto-) Colorado Plateau.

Crustal thickness and palaeo-elevation are intrinsically linked and can be calculated from each other assuming isostatic equilibrium of the lithospheric column. Palaeo-elevation estimates for Colorado Plateau region—and thus its uplift history—integrate a wide range of geomorphologically or environmentally sensitive criteria, including botanical evidence; vesicle morphology in erupted basalts; integrated marine depositional ages, local relief inferred from (U–Th)/He dating, and calculated palaeo-elevation of lacustrine sedimentary rocks; a thermochronology-based reconstruction of crystalline-basement exposure for the Upper Granite Gorge, Grand Canyon region; calculated changes in dynamic topographic uplift inferred from reconstructed sub-lithospheric mantle-flow models; and a cumulative reconstruction of the plateau region calculated by inverse modelling of longitudinal river profiles (Flowers et al., 2008; Huntington et al., 2010; Moucha et al., 2009; Roberts et al., 2012; Sahagian et al., 2002; Wolfe et al., 1997). Most of these techniques support a period of significant of uplift at the Oligocene–Miocene boundary (∼25 Ma), coincident with volcanism in the Four Corners region. Most tectonic models of the uplift of the Colorado Plateau invoke a dependence on flat-slab subduction of the Farallon plate beneath the plateau region during the Cenozoic. Most support Oligocene–Miocene 'epeirogenic' uplift associated with regional extension via convective removal of lithosphere or conductive heating from below, and some suggest an additional period of early (∼80–40 Ma; Late Cretaceous–Early Cenozoic) uplift due to regional shortening and homogenous crustal thickening (Bird, 1979; Humphreys et al., 2003; McQuarrie & Chase, 2000; Parsons & McCarthy, 1995; Thompson & Zoback, 1979). Additional models propose mid-Cenozoic uplift related to delamination of the Farallon plate, thus adding buoyancy to the upper mantle by mechanical thinning or chemical modification of the lithosphere, or the influence of a mantle plume (Parsons & McCarthy, 1995; Roy et al., 2005; Spencer, 1996).

3 | METHODOLOGY

We conducted a systematic, tectonic process-oriented quantification of the potential for subduction-devolatilization-derived aqueous fluids to metasomatize and isostatically uplift continental crust. We focus on intraplate regions that overlie zones of significant aqueous-fluid release associated with low-angle-subducting oceanic lithosphere, which establishes a trench-proximal to trench-distal framework of greenschist to blueschist facies metamorphism and consequent potential for crustal hydration far from plate margins. This process-oriented approach necessitates a quantitative estimate of the potential supply of H_2O fluid (expelled from a subducting slab; see Figure 1a,c) that fluxes across the Moho and into continental crust, described by the parameter Q' [kg m^{-2} Myr^{-1}] (Section 3.1; Appendix A). We then model the petrophysical effects of crustal hydration—including isostatic surface uplift, Δh [km]—both as a minimally hydrated, closed system (Section 3.2.1) and as a variably hydrated, open system that uses the input parameter Q [kg m^{-2}] to describe the cumulative mass of H_2O that infiltrates the crust (Section 3.2.2; Appendices B–D). Finally, we normalize our model Q values by our estimated Q' values to estimate the duration [Myr] over which subducting, dewatering oceanic slabs supply H_2O fluid to hydrate and isostatically uplift overlying continental crust by a given Δh magnitude [km] (section 3.3). Model properties discussed in this text are summarized in Table 1.

3.1 | How much water can subducting oceanic slabs supply to overlying continental crust?

The upward buoyancy-driven basal flux of subduction-derived aqueous fluids across the Moho—Q' [kg m^{-2} Myr^{-1}]—governs the extent of metasomatism in the overlying continental crust (Figure 1a). H_2O loss from subducting slabs is itself controlled by subduction zone variables including slab dip, slab age, plate velocity, sediment thickness, and extent of shear heating along the subduction interface. Integrated petrological and thermo-kinematic modelling for 56 global subduction zone segments suggests that modern subducting oceanic slabs

TABLE 1 Variables used and discussed in this study.

Usage	Variable	Unit(s)	Property
Slab dehydration	θ	°	Slab dip
	dX	m	Slab-segment width (strike-parallel)
	dY	km	Pre-arc Moho length (strike-normal)
	dZ	km	Pre-arc depth range
	$q'dX$	10^9 kg m^{-1} Myr^{-1}	Slab H_2O loss
	Q'	10^6 kg m^{-2} Myr^{-1}	Moho H_2O flux
Model geotherm, petrological-isostatic modelling	T_0	°C	Surface temperature
	q_0	mW m^{-2}	Surface heat flow
	A	μW m^{-3}	Radiogenic heat production
	k	W m^{-1}°C^{-1}	Thermal conductivity
	P	kbar	Pressure
	T	°C	Temperature
	z	km	Depth
	dz_{node}	m, km	Crustal node thickness
	dz	km	Crustal column thickness
	X	wt%	Bulk-rock composition
	H_2O	wt%	Mineral H_2O content
	Q	10^6 kg m^{-2}	Moho H_2O infiltration
	ρ	g cm^{-3}	Bulk-rock density
	$\Delta\rho$	%, g cm^{-3}	Bulk-rock density contrast
	Δh	km	Cumulative isostatic surface uplift
	δh	%, m	Single-node isostatic uplift

expel 2.6–23.2 × 10^9 kg Myr^{-1} m^{-1} H_2O from pre-arc depths (40–120 km) along a 1 m strike-parallel slab length over a 1 Myr duration (Dataset S1) (Abers et al., 2020; van Keken et al., 2011). Using slab-dip angles to project H_2O loss from subducting oceanic slabs onto overlying Moho surfaces (Appendix A) suggests that they supply averages of $Q' = 0.03–0.65 \times 10^6$ kg m^{-2} Myr^{-1} H_2O that may potentially flux into the overlying crust (Figure 1c) (Syracuse et al., 2010). Our projected Q' values (Figure 1c) are maximum estimates because they ignore metasomatism of the intervening mantle wedge, which consumes upward-percolating H_2O and reduces its flux into the lower crust. Global Q' values positively correlate with slab dip, θ [°], and span the lowest and narrowest range ($Q' = 0.03–0.12 \times 10^6$ kg m^{-2} Myr^{-1}) for low-angle slabs ($\theta = 10–34°$) such as Cascadia, which underlie thinner mantle wedges than high-angle slabs (Dataset S1). Those that subduct beneath continental lithosphere provide modern representations of the ancient, low-angle Farallon oceanic plate during the Laramide orogeny.

3.2 | Metasomatism-induced plateau uplift: closed- and open-system petrological modelling

The surface-uplift effect of metasomatic reactions in the deep continental crust can be investigated under both closed- ('static') and open-system ('dynamic') end-member hydration scenarios. The 'static' case considers the instantaneous introduction of aqueous fluid into a rock for a given depth range within the continental crust and is the most common form of modelling used to assess the petrophysical effects of in situ metamorphic hydration. Such models represent a closed system that instantaneously changes its state before and after a hydration event and provide a useful reference for open-system models that consider the more geologically realistic scenario of incremental addition or consumption of fluid over dynamically varying length scales. We therefore integrate closed- and open-system modelling, as discussed below. Aqueous fluids in both modelling frameworks infiltrate the crustal upper plate of a subduction system and are derived from the subducting, dewatering lower plate. We assume that aqueous fluids, during their transport from the lower plate to the upper plate, do not react with the mantle to form hydrous minerals or induce melting. We justify this assumption despite its possible deviation from reality because it enables us to consider focused, end-member scenarios that test the effects of crustal hydration based on contextualized and quantified supplies of aqueous fluids that drive the process.

3.2.1 | Closed-system petrological modelling: a basis for reference

Our closed-system petrological models quantify interrelationships among bulk rock chemistry (X), pressure (P), and temperature (T) (Appendix C). All models were run along a ~13°C/km geotherm that is representative of bulk-average, non-deforming continental crust and was determined based on one-dimensional (1-D) steady-state heat conduction with volumetric heat production (Appendix B, Dataset S2). This geotherm passes through sub-greenschist-facies conditions in the upper crust, greenschist facies in the middle crust, and epidote-amphibolite to amphibolite (or low-temperature/high-pressure granulite) facies in the lower crust. The activity–composition relations that we implemented in our models are specified in Table 2. We consider three lithologies to represent the lower ($z = 40–23$ km) and middle ($z = 23–12$ km) continental crust (Table 3): a metabasite representative of the lower crust, as determined by granulite xenoliths exhumed within diatremes in the central Colorado Plateau; a granodiorite representative of intermediate–felsic lower–middle continental crust; and a metapelite representative of metasedimentary middle continental crust (Ague, 1991; Condie & Selverstone, 1999; Le Maitre, 1976). The upper crust (z = 12–0 km) was not considered in this modelling.

We considered both nominally anhydrous (~0.5 mol.% H_2O free water total) and minimally hydrated (~1 mol.% free H_2O at the first point of melting along our extrapolated geotherm) fluid contents prior to metasomatism, following the model setup of Wade et al. (2017). These hydration states are intended to represent end members for continental crust in nature. Although first-generation sediments experiencing burial (during orogenesis, for example) are likely to be fluid-saturated, older crust (e.g., in cratons) is likely to be drier, especially throughout its lower–middle depths. This treatment in our models enables us to examine this range of natural states. Forward modelling of metamorphic reactions enables calculation of density changes ($\Delta\rho$) before and after hydration, which we use to calculate the magnitude of isostatic adjustment at Earth's surface (Δh) (Appendix D). Full model results are provided in Dataset S3.

3.2.2 | Open-system petrological modelling: an attempt to simulate upward-propagating hydration into the crust

We focus our present contribution on open-system ('dynamic') hydration scenarios involving reactive transport to analyse the potential for lower–middle-crustal

TABLE 2 Solid-solution models used for phase-equilibrium modelling with *Perple_X*.

Mineral or phase	Abbreviation[a]	Metabasite	Granodiorite	Metapelite	Composite crust	Solution model name	Reference
Garnet	Grt	X	X	X	X	Gt (W)	White et al. (2014)
Feldspar	Fsp	X	X	X	X	Fsp (C1)	Holland and Powell (2003)
Clinopyroxene	CPx	X	X	X	X	Omph (GHP)	Green et al. (2007)
Orthopyroxene	Opx	X	-	-	X	Opx (W)	White et al. (2014)
Amphibole	Amp	X	X	X	X	cAmph (G)	Green et al. (2016)
Biotite	Bt	X	X	X	X	Bi (W)	White et al. (2014)
White mica	Wm	X	X	X	X	Mica (W)	White et al. (2014)
Staurolite	St	-	-	X	X	St (W)	White et al. (2014)
Chloritoid	Cld	-	-	X	X	Ctd (W)	White et al. (2014)
Cordierite	Crd	-	X	X	X	Crd (W)	White et al. (2014)
Chlorite	Chl	X	X	X	X	Chl (W)	White et al. (2014)
Epidote	Ep	X	X	X	X	Ep (HP11)	Holland and Powell (2011)
Ilmenite	Ilm	X	X	X	X	Ilm (WPH)	White et al. (2014)
Melt	Melt	X	X	X	X	melt(G)	Green et al. (2016)

[a] Following Whitney and Evans (2010) and used for Figures 3, 6, and 8.

metasomatism to drive intracratonic surface uplift. In this scenario, a 1-D rock column may be subject to geodynamic perturbations that introduce aqueous fluids from either internal or external sources, for example, water released during devolatilization of subducting oceanic lithosphere (Figure 1a,b). These mobile fluid phases move upward through the column until they are either consumed by hydration reactions or pass through the top of the column and out of the system. Metamorphic phase relations can be calculated at any depth within the column following interaction with a given mass of fluid percolating towards the surface, allowing a metasomatic front to be progressively 'traced' in absolute space and relative time. The mobile fluids therefore interact with a rock column as they migrate through it, changing the local bulk composition and mineralogy of the petrological system during percolation.

Our open-system models quantify interrelationships among cumulative H_2O infiltration across the Moho (Q), bulk-rock chemistry (X), pressure (P), and temperature (T) (Appendix C). We use the same model geotherm (~13°C/km; Appendix B), activity–composition relations (Table 2), and nominally anhydrous model lithologies (metabasite, granodiorite, and metapelite; Table 3) from our closed-system models for our open-system models and apply the same density-change ($\Delta\rho$) and isostatic-uplift (Δh) calculations (Appendix D). The exception for our open-system models is a multi-lithological crust model (discussed below).

Although mono-lithologic columns provide insight into the metamorphic behaviour of key crustal rock types during progressive hydration, geophysical and geological studies of the continental crust suggest that mafic rocks are most common in the lower crust, intermediate–felsic rocks are most common in the middle and uppermost lower crust, and pelitic rocks are most common in the upper middle crust (Rudnick & Gao, 2003). Thus, we provide an additional set of models for a composite lithological column that integrates our metabasite ($z = 40$–27 km), granodiorite ($z = 27$–20 km), and metapelite ($z = 20$–12 km) lithologies (Table 3). Our model composite crust represents differentiated, stable continental crust akin to the proto-Colorado Plateau prior to Cenozoic uplift. Full model results are provided in Dataset S3.

3.3 | Absolute temporal framework

Although petrological reactive-transport modelling predicts progressive petrophysical changes as a consequence of incremental fluid infiltration through a crustal column, it cannot currently account for the timescales over which these processes occur. This limitation restricts reactive-transport modelling to a time-integrated reference frame [mass area^{-2}] for fluid infiltration (Q), which precludes our ability to directly predict the petrophysical changes associated with a strictly defined mass flux [mass time^{-1} area^{-2}] of aqueous fluid across the Moho and into

TABLE 3 Model bulk compositions for lithologies used in this study.

Model lithology	Modelled depth in composite crust	Hydration state[a]	SiO_2	Al_2O_3	CaO	MgO	FeO	K_2O	Na_2O	TiO_2	MnO	H_2O	O	Total	X_Fe^{3+}	X_Mg
Metapelite	20–12 km	Nominally anhydrous	58.23	20.89	1.34	3.34	8.67	4.16	1.86	1.09	0.00	0.13	0.29	100.00	0.15	0.41
		Minimally hydrated	56.68	20.34	1.30	3.25	8.44	4.05	1.81	1.06	0.00	2.78	0.28	100.00		
Granodiorite	27–20 km	Nominally anhydrous	67.19	15.96	3.65	1.77	4.02	2.77	3.81	0.55	0.00	0.14	0.13	100.00	0.15	0.44
		Minimally hydrated	66.05	15.69	3.59	1.74	3.96	2.73	3.75	0.54	0.00	1.83	0.13	100.00		
Metabasite	40–27 km	Nominally anhydrous	52.71	16.43	8.24	6.05	10.52	1.37	3.20	0.95	0.00	0.14	0.38	100.00	0.16	0.51
		Minimally hydrated	51.76	16.14	8.09	5.94	10.33	1.35	3.14	0.93	0.00	1.95	0.37	100.00		

Note: Oxides are provided in w.%. Minimally hydrated compositions are provided for reference.

[a] Nominally anhydrous compositions from Condie and Selverstone (1999), Le Maitre (1976), and Ague (1991). Minimally hydrated compositions defined as those with <1 mol.% H_2O at the first point of melting extrapolated along our 13°C/km geotherm.

a crustal column at a prescribed rate (Q'). Surface-uplift estimates based on reactive-transport models therefore require independent temporal constraints to be useful for a quantitative understanding of regional-tectonic processes, which themselves are commonly described in an absolute-temporal framework bracketed by radio-isotopic dating and numerical modelling.

We integrated the time dimension into our models through the use of independently constrained fluid-release rates from the subducting slab. Our estimates of subduction-devolatilization-derived H_2O fluid flux across the Moho (Q') (Figure 1c) were used to benchmark our reactive-transport models (Figure 1b), which involve cumulative (albeit incremental) H_2O fluid infiltration across the Moho (Q) and upwards through continental crust. More specifically, we normalize our model Q values, which are associated with predicted surface-uplift magnitudes (Δh), by our projected Q' values, which are associated with given subduction scenarios and H_2O fluid supply. This produces an absolute timeframe [Myr] over which surface uplift [km] develops due to incremental infiltration of a cumulative mass of H_2O fluid across the Moho [kg m^{-2}] and into continental crust from an underlying, subducting, and dewatering oceanic slab. Equivalently, we can predict surface-uplift magnitude [km] based on the flux of aqueous fluids [kg m^{-2} Myr^{-1}] into the base of a crustal column [m^2] over a given duration [Myr]. We use the modern Cascadia slab and our model composite crust as an analogue to the ancient Farallon slab and the Colorado proto-Plateau crust to illustrate this concept (section 5.1.1).

4 | MODELLING RESULTS

4.1 | Closed-system models: monolithologic reference crustal columns

Stable mineral assemblages, bulk-rock densities, and mineralogically bound H_2O for all three nominally anhydrous model lithologies are shown in Figure 3a,c,e. Calculated assemblages in each lithology reflect the P–T geotherm, which passes through sub-greenschist-facies conditions in the upper crust, greenschist facies in the middle crust, and epidote-amphibolite to amphibolite (or low-temperature/high-pressure granulite) facies in the lower crust. Among the nominally anhydrous lithologies, bulk-rock densities are greatest for metabasite ($\rho = 3.15$–3.30 g cm^{-3}; Figure 3e), lowest for granodiorite ($\rho = 2.81$–2.85 g cm^{-3}; Figure 3c), and intermediate for metapelite ($\rho = 3.01$–3.04 g cm^{-3}; Figure 3a). Garnet and feldspar modal abundances exert the most significant influence on density for each lithology. Metabasite

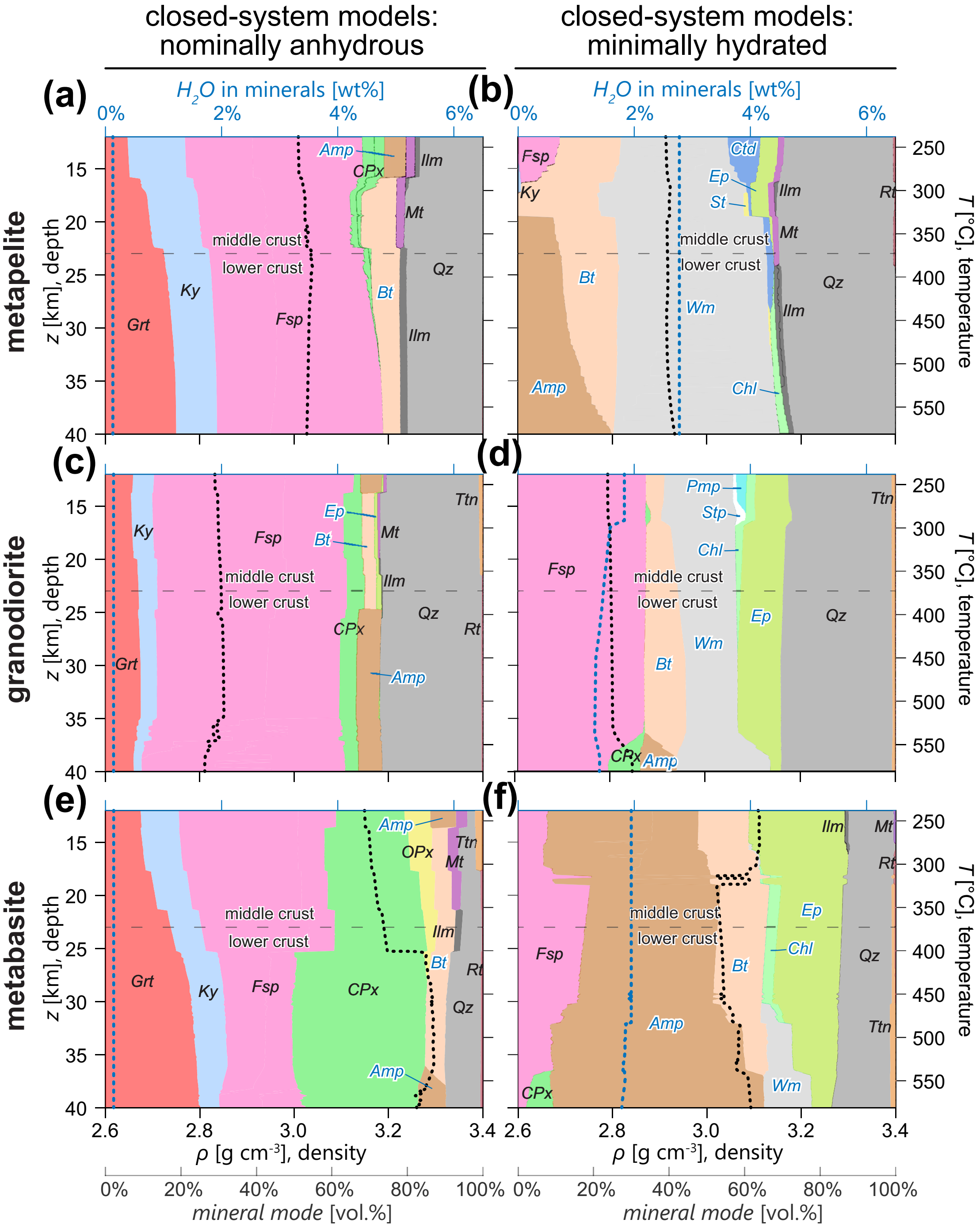

FIGURE 3 Mineral proportions [vol.%] in nominally anhydrous and minimally hydrated continental crust. Equilibrium phase relations are shown for metapelite (a, b), granodiorite (c, d), and metabasite (e, f) on the left-hand- and right-hand-side panels for nominally anhydrous and minimally hydrated lithologies. Bulk-rock density (black dashed line) and the total fluid content of hydrous minerals (blue dashed line) are shown for reference. Mineral labels are abbreviated following Whitney and Evans (2010), and are coloured black for anhydrous and blue for hydrous varieties. Model nodes are ~140 m thick.

exhibits the greatest variability in density (up to 0.15 g cm^{-3}; Figure 3e), which is controlled by increasing garnet and decreasing feldspar modal abundance with depth; a downward 0.08 g cm^{-3} density increase at ~25 km depth corresponds to an additional increase in clinopyroxene modal abundance at the expense of feldspar. Granodiorite density varies little with depth (up to 0.04 g cm^{-3}; Figure 3c) due to roughly constant garnet and feldspar modal abundances above ~35 km; lower garnet and greater feldspar modal abundances below ~35 km contribute to a downward density decrease. Metapelite density also varies little with depth (up to

$0.03\ \mathrm{g\ cm^{-3}}$; Figure 3a), especially in the lower crust (23–40 km), where increasing garnet and feldspar modal abundances negate any change in bulk-rock density.

Mineral assemblages, bulk-rock densities, and non-fluid H_2O content for minimally hydrated model lithologies are shown in Figure 3b,d,f. Metapelite requires the most H_2O to become minimally hydrated (2.8 wt%; Figure 3b) compared with metabasite (1.8–1.9 wt%; Figure 3f) and granodiorite (1.3–1.8 wt%; Figure 3d). Hydrous minerals are nevertheless most abundant in metabasite (67–81 vol.%) compared with metapelite (58–72 vol.%) and granodiorite (36–38 vol.%). Bulk-rock densities for the minimally hydrated lithologies are significantly lower than those for their nominally anhydrous counterparts, which have only 4–9 vol.% hydrous minerals. Metabasite density (Figure 3f) is greatest from 12–18 km depth ($\rho = 3.11\ \mathrm{g\ cm^{-3}}$) due to high amphibole + epidote and low feldspar modal abundances; it spans $3.02–3.09\ \mathrm{g\ cm^{-3}}$ below 18 km depth, with which it increases due to increasing amphibole + clinopyroxene and decreasing feldspar abundances. Granodiorite density (Figure 3d) is roughly constant from 12–37 km depth ($\rho = 2.79–2.80\ \mathrm{g\ cm^{-3}}$) due to constant modal abundances of major minerals; it increases from 37–40 km to $2.81–2.84\ \mathrm{g\ cm^{-3}}$ due to increasing clinopyroxene + amphibole and decreasing feldspar modal abundances. Metapelite density (Figure 3b) is remarkably constant throughout the entire middle and lower crust ($\rho = 2.91–2.93\ \mathrm{g\ cm^{-3}}$).

Model density contrasts and isostatic-uplift estimates due to instantaneous hydration of the mono-lithologic crustal columns correspond in rank to the modal abundances of hydrous minerals produced in each lithology (Figure 4). The most significant density reduction occurs for minimally hydrated metabasite from 40–19 km depth, where replacement of garnet, clinopyroxene, and kyanite by hydrous minerals reduces bulk-rock density by 5%–8% and drives ~1.3 km of cumulative isostatic surface uplift (Figure 4e,f). Metapelite hydration reduces its density by a lower magnitude (3%–4%) across its modelled depth range and drives ~0.9 km of cumulative isostatic surface uplift (Figure 4a,b). Granodiorite hydration produces the lowest-magnitude density reduction of all three lithologies (1%–2% above 37 km) and drives ~0.3 km of cumulative isostatic surface uplift (Figure 4c,d).

4.2 | Open-system models: mono-lithologic reference crustal columns

The vertical extent of fluid infiltration into idealized crustal columns composed of nominally anhydrous metabasite, granodiorite, and metapelite is shown in Figure 5 and summarized in Table 4, and the mineralogical changes associated with hydration at low ($Q = 0.2 \times 10^6\ \mathrm{kg\ m^{-2}}$) and high ($Q = 0.8 \times 10^6\ \mathrm{kg\ m^{-2}}$) cumulative infiltration are shown in Figure 6. For all rock types, metasomatism penetrates further up through the column in proportion to the magnitude of Q, with metapelitic rocks incorporating the most H_2O beyond minimal hydration (2.8–4.0 wt%) compared with granodiorite (1.8–2.1 wt%) and metabasite (1.9–3.0 wt%) (Figure 5a,c,e). For relatively low H_2O infiltration magnitudes ($Q = 0.2 \times 10^6\ \mathrm{kg\ m^{-2}}$), mineralogical transformation occurs within the lowermost ~3, ~6, and ~5 km of metapelitic, granodioritic, and metabasic continental crust, respectively, with anhydrous garnet, kyanite, clinopyroxene, and/or feldspar in felsic and low-temperature/high-pressure mafic granulite reacting to form hydrous clinoamphibole, white mica, biotite, and/or epidote (Figure 6a,c,e). These changes cause a reduction in density on the order of $0.15–0.3\ \mathrm{g\ cm^{-3}}$ ($\Delta\rho$ up to -7.0%) across the hydration front, although the low Q magnitude restricts all metasomatism to the base of the lower crust, such that the majority does not undergo transformation (Figure 7a,c,e).

For higher H_2O infiltration magnitudes ($Q = 0.8 \times 10^6\ \mathrm{kg\ m^{-2}}$), aqueous fluid infiltration and associated metasomatism occur within the lowermost ~9 and ~14 km of the crust in metapelitic and metabasic lithologies (Figure 6b,f), respectively, but penetrate ~23 km upwards for granodiorite, thus also affecting the middle crust (Figure 6d). Akin to low-Q transformations, garnet, kyanite, and clinopyroxene are almost completely transformed into hydrous clinoamphibole, white mica, chlorite, and epidote, causing a reduction in density of up to $0.13\ \mathrm{g\ cm^{-3}}$ ($\Delta\rho = -4.3\%$) for metapelite and up to $0.32\ \mathrm{g\ cm^{-3}}$ ($\Delta\rho = -10\%$) for metabasite across the hydration front (Figure 7a,e). Granodiorite, however, shows a much smaller reduction in density of up to $0.05\ \mathrm{g\ cm^{-3}}$ ($\Delta\rho = -1.8\%$; Figure 7c).

Isostatic-uplift-potential estimates are shown and summarized in Figure 7 and Table 4 for Q values of 0.2 and $0.8 \times 10^6\ \mathrm{kg\ m^{-2}}$. Single-node isostatic uplift (δh, absolute magnitude for a node normalized to 273 m node thickness; Appendix D) due to hydration can reach 7%–10% in garnet- and pyroxene-rich, amphibolite-facies metabasic assemblages that transform to lower-density amphibole-, epidote-, mica-, and chlorite-rich assemblages, which induces up to ~1 km of cumulative surface uplift for $Q = 0.8 \times 10^6\ \mathrm{kg\ m^{-2}}$ (Figure 7f). Similar mineralogical transformations occur for low Q values ($0.2 \times 10^6\ \mathrm{kg\ m^{-2}}$), but these minor magnitudes of aqueous fluid infiltration do not permit infiltration to significant heights within the crust because all volatiles are consumed during ascent before fluid saturation can occur.

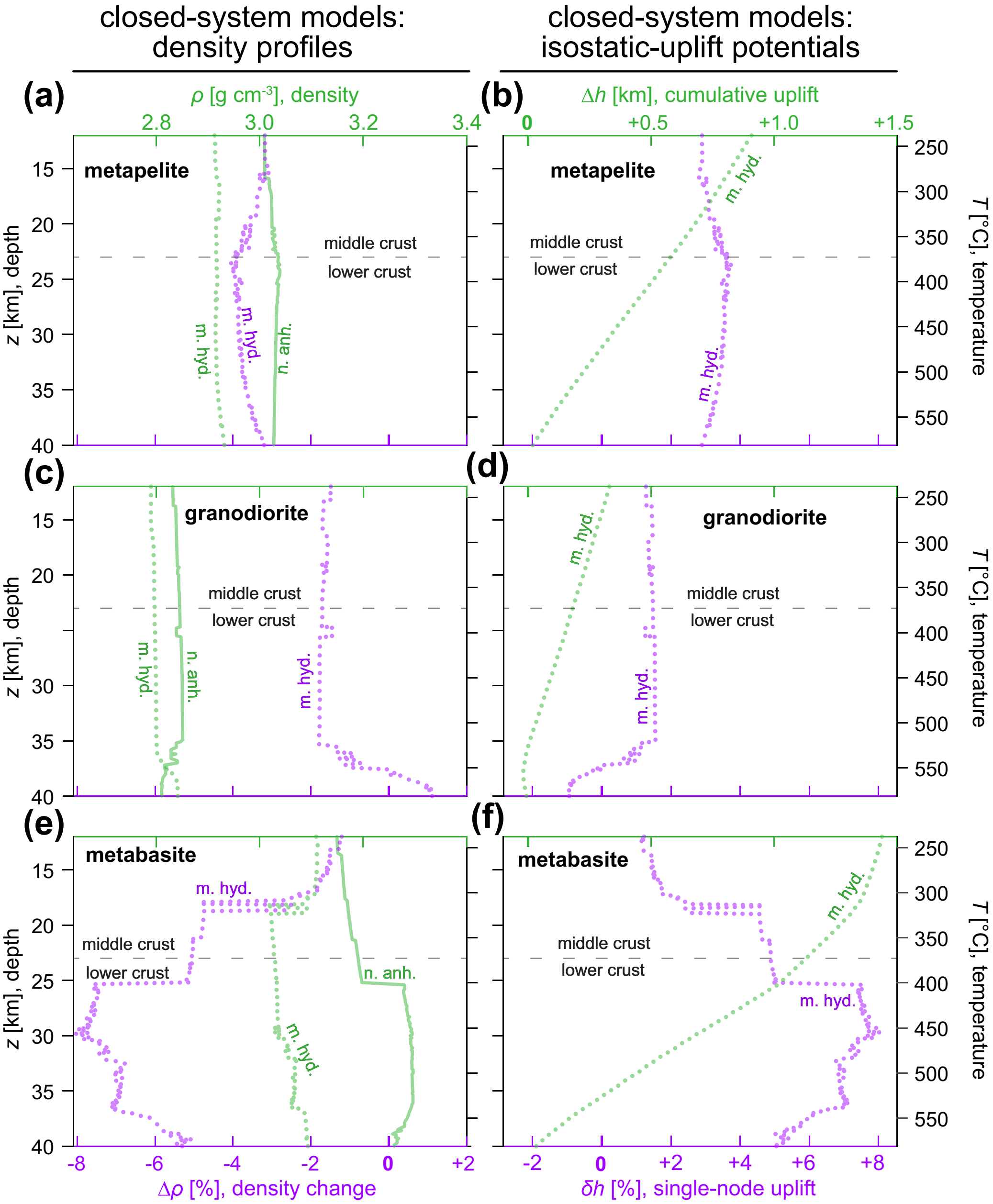

FIGURE 4 Magnitudes of de-densification and surface uplift for instantaneously hydrated continental crust. Left-hand side panels (a, c, e) show absolute value of density, ρ [g cm^{-3}] in green and percentage change in density, $\Delta\rho$ [%] in purple, caused by metasomatic reactions in each rock type at different crustal levels. Right-hand side panels (b, d, f) show cumulative isostatic surface uplift, Δh [km] in green and single-node isostatic uplift, δh [%] in purple after minimal hydration of nominally anhydrous crust. Model nodes are ~140 m thick, and single-node uplift is normalized to node thickness. n. anh., nominally anhydrous; m. hyd, minimally hydrated.

4.3 | Open-system models: composite crustal column

Aqueous fluid infiltration into the base of our model composite crust hydrates and de-densifies it identically to the corresponding depth range ($z = 40$–27 km) for our metabasite crustal column (Figure 8a–b; Table 4). Infiltration of H_2O into the granodioritic lower–middle crust ($z = 27$–20 km) only occurs for $Q > 0.7 \times 10^6$ kg m^{-2}, and none reaches the metapelitic upper crust ($z = 20$–12 km) for our modelled Q range (Figure 8a). Granodioritic crust ($z = 27$–20 km) is markedly less dense than subjacent metabasite (<0.5 g cm^{-3}), albeit to lower magnitudes (<0.2 g cm^{-3}) if the hydration front reaches its base (Figures 8c,d). Metasomatic reactions are predicted to cause local density reductions of up to 10% (Figures 8b, e), producing a maximum cumulative surface uplift of Δh ~1 km for $Q = 0.8 \times 10^6$ kg m^{-2} (Figure 8f).

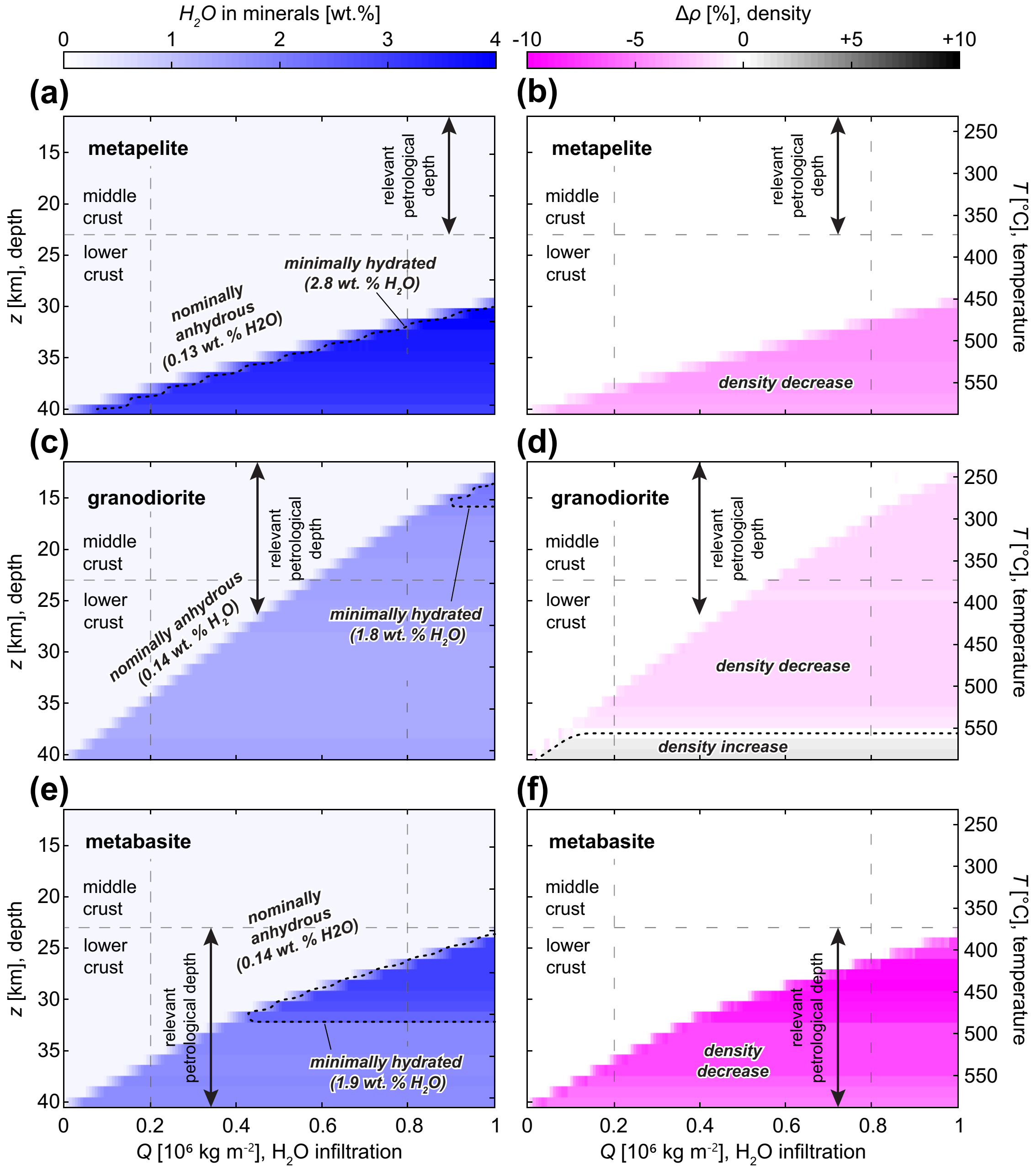

FIGURE 5 Crustal hydration magnitudes calculated via open-system reactive-transport modelling. Model results show the degree of hydration at various depths (z) within the considered crustal column due to infiltration of aqueous fluid at its base. Left-hand side panels (a, c, e) show the fluid content, H_2O [wt%], in the three studied rock types in z–Q space, and right-hand side panels (b, d, f) show the percentage changes in density, $\Delta\rho$ [%], caused by metasomatic reactions. Vertical dashed lines for $Q = 0.2$ and 0.8×10^6 kg m^{-2} correspond to modelled H_2O-infiltration magnitudes in Figures 6, 7, and 8. Model nodes are 1 km thick.

5 | DISCUSSION

Our reactive-transport modelling framework quantifies the petrophysical changes and surface-uplift expressions resulting from the ideal, 100%-efficient interaction between nominally anhydrous continental crust and variable magnitudes of upward-percolating aqueous fluid. Our models show that metabasic, amphibolite-facies continental lower crust experiences the largest reduction in density (~10%) due to hydration, caused primarily by the breakdown of garnet and clinopyroxene to amphibole, white mica, and epidote (Figure 6e,f). The extent of surface uplift due to de-densification of a 13 km-thick metabasite layer ($z = 40$–27 km) in the lower crust shows a pseudo-linear relationship with the cumulative mass of fluid infiltration (Q), with isostatic-uplift potentials between ~0.3 and ~1 km for low ($Q = 0.2 \times 10^6$ kg m^{-2}) and high ($Q = 0.8 \times 10^6$ kg m^{-2}) fluid-infiltration

TABLE 4 Summarized results for open-system, reactive-transport petrological models for fluid-infiltration magnitudes of $Q = 0.2 \times 10^6$ and 0.8×10^6 kg m^{-2} ($Q = 0.2$ and $Q = 0.8$).

	Depth range of metasomatism		**Max. hydration in model crust**		**Max. density contrast in model crust**				**Cumulative isostatic surface uplift**	
	z [km]		**H_2O_{max} [wt%]**		**$\Delta\rho_{max}$ [g cm^{-3}]**		**$\Delta\rho_{max}$ [%]**		**Δh [km]**	
	$Q = 0.2$	$Q = 0.8$	$Q = 0.2$	$Q = 0.8$	$Q = 0.2$	$Q = 0.8$	$Q = 0.2$	$Q = 0.8$	$Q = 0.2$	$Q = 0.8$
Metapelite	40–37	40–31	3.1%	3.6%	−0.11	−0.13	−3.7%	−4.3%	0.1	0.3
Granodiorite	40–34	40–17	1.4%	1.6%	−0.05	−0.05	−1.8%	−1.8%	0.0	0.3
Metabasite	40–35	40–26	1.8%	3.0%	−0.23	−0.32	−7.0%	−9.7%	0.3	1.0
Composite	40–35	40–25	1.8%	3.0%	−0.23	−0.32	−7.0%	−9.7%	0.3	1.0

Note: Reported maximum density contrasts are the most negative values for each model.

magnitudes, respectively (Figure 7e,f). By contrast, the middle continental crust ($z = 23$–12 km) is characterized by granodioritic and metapelitic lithologies, and metasomatism is only likely to infiltrate this shallower depth range if cumulative fluid infiltration is sufficiently high ($Q > 0.8 \times 10^6$ kg m^{-2}; Figure 8a) such that the lower crust does not completely consume the entirety of free aqueous fluid during its ascent. Therefore, dewatering slabs are not expected to drive significant metasomatic transformation of the overlying middle (granodioritic and pelitic) crust, limiting its potential to contribute to surface uplift.

5.1 | Application of our models to the Colorado Plateau

5.1.1 | How fast and by what magnitude could the dewatering Farallon slab have contributed to Colorado Plateau uplift?

Given the surface-uplift responses to time-integrated H_2O fluid infiltration into continental lower crust quantified above, we use previous estimates of H_2O loss from the modern Cascadia slab—our analogue for the ancient, low-angle Farallon slab—to interrogate the potential for lower-crustal hydration to uplift the Colorado Plateau (Abers et al., 2020; Syracuse et al., 2010; van Keken et al., 2011). In this scenario, the pre-arc component of the dewatering, 20°-dipping Cascadia slab underlies a ~220 km, strike-perpendicular length of our model composite crust and supplies a projected, surface-averaged basal flux of H_2O through its Moho of $Q' = 0.05 \times 10^6$ kg m^{-2} Myr^{-1} (Figure 1). This basal H_2O mass flux predicts cumulative surface uplift of ~0.3 and ~1 km ($Q = 0.2 \times 10^6$ kg m^{-2} and 0.8×10^6 kg m^{-2}) after 4 and 16 Myr (Figure 8f). Corresponding surface-uplift rates are ~70 and ~60 m Myr^{-1}. The surface-uplift durations and rates are respectively minimum and maximum estimates because our projected Q' values ignore mantle metasomatism, which renders them maximum estimates of H_2O fluid flux through the Moho.

5.1.2 | Metasomatism of sub-Colorado Plateau lithospheric mantle

The lithospheric mantle beneath the Colorado Plateau is significantly more hydrated than that beneath other cratonic regions worldwide (Chin et al., 2021; Li et al., 2008). This high H_2O content was previously proposed to account for its relatively thin lithosphere (~120–150 km) compared with the North America Craton (>200 km), which poses a testable hypothesis (Lee et al., 2011; Levander et al., 2011). If most Farallon-slab-derived H_2O was accommodated in overlying mantle lithosphere that was subsequently delaminated or thinned, then the overlying lower crust should be relatively dry and hydration is unlikely to have driven surface uplift. However, if significant H_2O infiltrated the lower crust during the Laramide hydration event, then the lower crust should be atypically wet (relative to lower crust that has not been hydrated by an underlying, dewatering slab) and hydration-induced de-densification of lower crustal lithologies is predicted to significantly contribute to surface uplift (Butcher et al., 2017; Jones et al., 2015; Levandowski et al., 2018; Schulze et al., 2015; Smith et al., 2004).

The substantial degree of mantle metasomatism by aqueous fluids beneath the Colorado Plateau indicates voluminous infiltration of aqueous fluids and supports the feasibility of lower-crustal hydration to contribute to its uplift. In particular, mantle metasomatism to the extent of saturation may effectively neutralize a chemical barrier and enable younger aqueous fluids to infiltrate the overlying Moho and lower crust if the fluid supply is

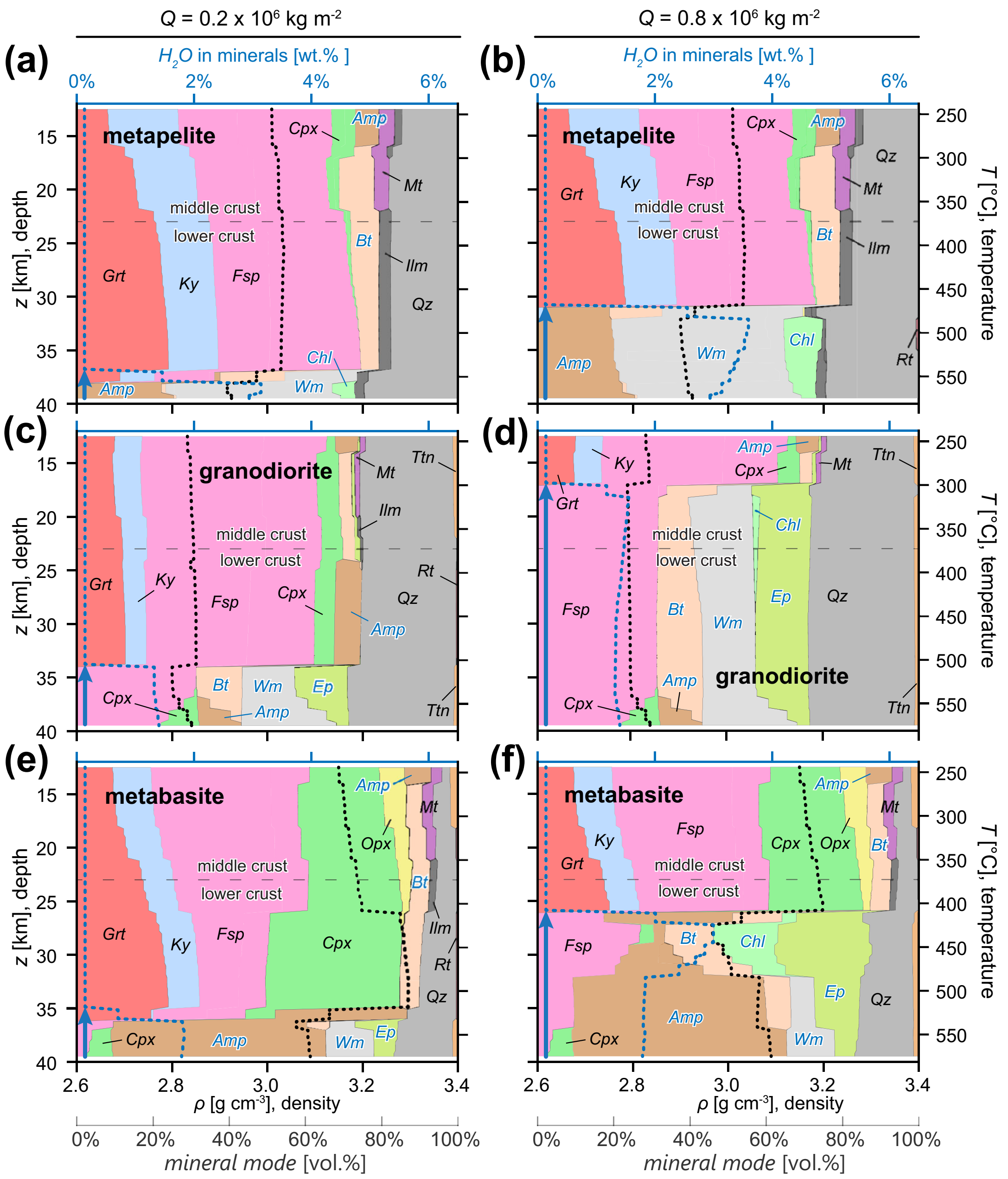

FIGURE 6 Mineral proportions (vol.%) in metasomatized continental crust above and below a vertically ascending hydration front. Equilibrium phase relations are shown for metapelite (a, b), granodiorite (c, d), and metabasite (e, f) on the left-hand and right-hand side panels for $Q = 0.2$ and 0.8×10^6 kg m^{-2}, respectively. Dark blue arrow marks the vertical distance over which metasomatism occurs for each rock type and fluid-infiltration scenario. Bulk-rock density (black dashed line) and the total fluid content of hydrous minerals (blue dashed line) above and below the hydration front are shown for reference. Only major mineral fields are labelled for clarity. Mineral abbreviations follow Whitney and Evans (2010). Model nodes are ~270 m thick.

sufficient. Furthermore, partial tectonic bulldozing of the lithospheric mantle beneath the Colorado Plateau by the low-angle Farallon slab would have reduced the thickness of mantle metasomatism that was necessary to permit H_2O fluid to infiltrate into the overlying lower crust (Hernández-Uribe & Palin, 2019a; Humphreys et al., 2015). Although the timescales for mantle metasomatism—a precondition for subduction-derived aqueous fluids to metasomatize the lower crust—are poorly known, the protracted duration over which the low-angle Farallon slab subducted and devolatilized beneath the Colorado Plateau implies a sustained, high-magnitude supply of aqueous fluids that render crustal metasomatism feasible despite the obstacles.

A simple approach to estimate the duration of low-angle subduction of the Farallon slab interprets ~80 Ma

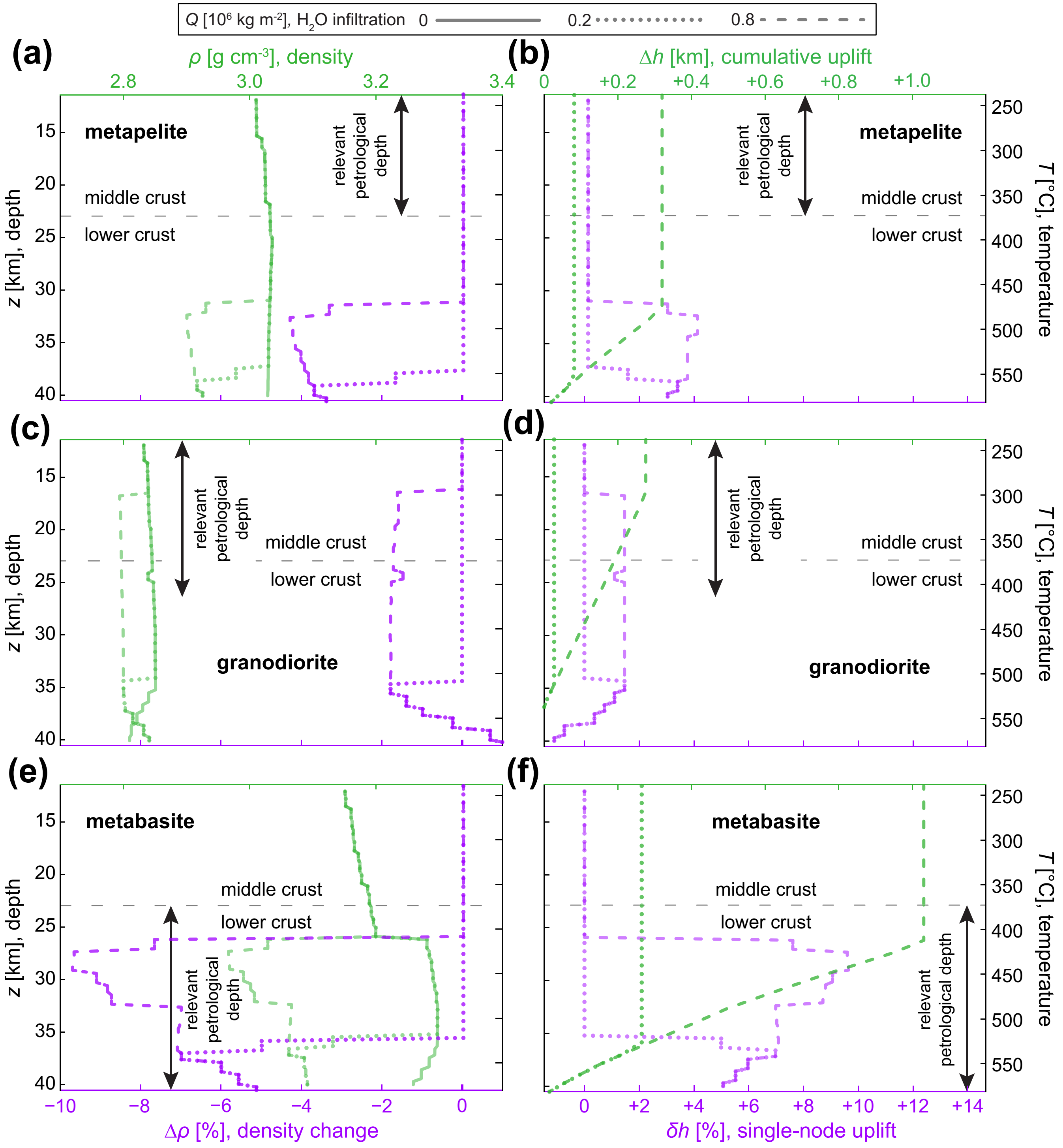

FIGURE 7 Magnitude of hydration-driven de-densification and surface uplift. Model results showing expected isostatic vertical surface uplift due to post-hydration volume expansion of lower and middle crust for two different fluid-infiltration scenarios ($Q = 0.2$ and 0.8×10^6 kg m^{-2}). Left-hand side panels (a, c, e) show absolute value of density, ρ [g cm^{-3}] in green and percentage change in density, $\Delta\rho$ [%] in purple, caused by metasomatic reactions in each rock type at different crustal levels. Right-hand side panels (b, d, f) show cumulative isostatic surface uplift, Δh [km] in green and single-node isostatic uplift, δh [%] in purple. Model nodes are ~270 m thick, and single-node uplift is normalized to node thickness. Q is time-integrated H_2O infiltration through a 1 m^2 horizontal Moho surface.

marine sediments on the plateau and the transition of western North America from a convergent to a transform margin at ~35 Ma as oldest and youngest age constraints (Atwater, 1970; Levander et al., 2011; Sahagian, 1987). This implies a ~45 Myr duration of Farallon-slab dewatering beneath the Colorado proto-Plateau, including a

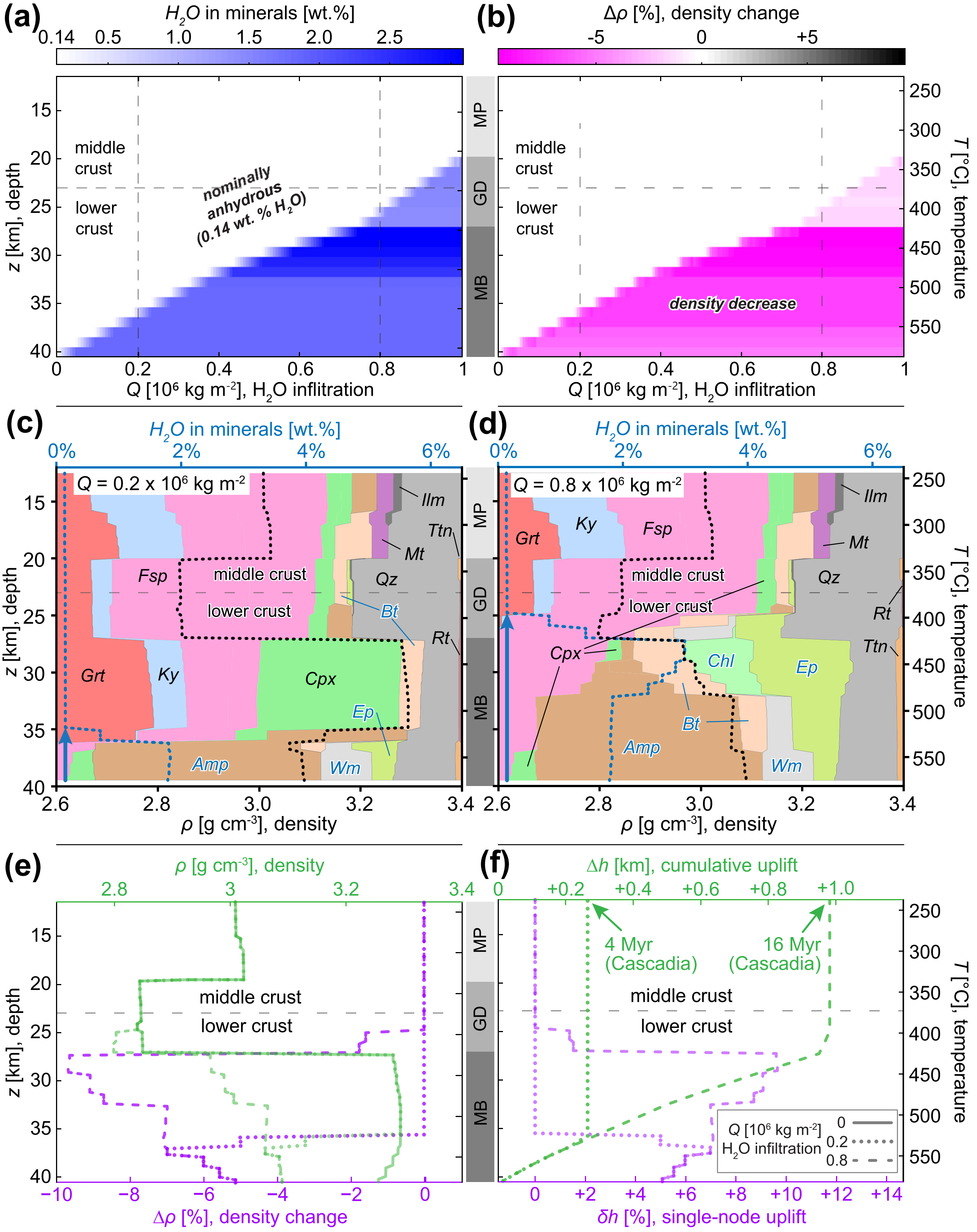

FIGURE 8 Legend on next page.

FIGURE 8 Hydration-induced changes in a composite continental crust at various depths (z) due to infiltration of aqueous fluids at its base. Top row shows (a) degree of hydration, H_2O [wt%] and (b) percentage change in density, $\Delta\rho$ [%]. Middle row (c, d) shows equilibrium phase relations for fluid-infiltration magnitudes of $Q = 0.2$ and 0.8×10^6 kg m^{-2}, with bulk-rock density, total fluid content of hydrous minerals, and mineral abbreviations as in Figures 3 and 6. Bottom row shows, for two different fluid-infiltration scenarios ($Q = 0.2$ and 0.8×10^6 kg m^{-2}), (e) absolute value of density, ρ [g cm^{-3}] in green and percentage change in density, $\Delta\rho$ [%] in purple, as well as (f) cumulative isostatic surface uplift, Δh [km] in green and single-node isostatic uplift, δh [%] in purple. Model nodes are 1 km thick (top row) or ~270 m thick (middle and bottom rows), and single-node uplift is normalized to node thickness. 4 and 16 Myr (Cascadia) highlight the durations required for the dewatering Cascadia slab to hydrate and drive ~0.3 and ~1 km of surface uplift of overlying continental crust. MB, metabasite; GD, granodiorite; MP, metapelite.

sustained supply of H_2O fluid to infiltrate the overlying mantle and continental crust. Assuming the modern, low-angle Cascadia slab is a suitable analogue for the ancient Farallon slab (Figure 1), the 16 Myr duration needed for its expelled H_2O fluid to hydrate and uplift the overlying Colorado Plateau by ~1 km (Figure 8f) implies that the intervening mantle must have been metasomatized and saturated within the preceding 29 Myr. Equivalently, this interpretation suggests that the Farallon slab subducted beneath the Colorado proto-Plateau for a duration ~2.8 times longer than that needed to metasomatize its lower crust and isostatically uplift its surface by ~1 km. Limitations of this back-of-the-envelope estimate are discussed in Section 5.3.

5.2 | Previous quantitative estimates of Colorado Plateau surface uplift

5.2.1 | Hydration-induced uplift

Closed-system, static petrological modelling of mafic lower crust beneath the Colorado Plateau predicts 0.3 km of hydration-de-densification-induced surface uplift and provides a useful comparison to our open-system, reactive-transport results (Porter et al., 2017). This 0.3 km isostatic-uplift estimate was based on a post-hydration density decrease of 0.06 g cm^{-3} (compared with our 0.15–0.3 g cm^{-3}) using the same mafic bulk-rock composition considered here, but for a single equilibrium assemblage with 0.7 wt% H_2O (compared with our 0–2.8 wt% H_2O) at 1 GPa and 700°C (compared with ~540°C for our model at equivalent depths) for a 16 km-thick layer (compared with our 13 km-thick layer) (Condie & Selverstone, 1999). The most significant factor driving greater surface uplift in our models is our overall greater H_2O content in minerals, especially between 32–27 km depth, where chlorite and epidote stability provide the maximum crustal-hydration magnitude in our column (Figure 8c,d). The chief advantage of our models is that they account for variable density contrast with depth in the crust, whereas closed-system modelling presumes uniformity with depth.

Geophysical determinations of lower-crustal density contrasts between the Great Plains and the Colorado Plateau–Rocky Mountains region corroborate the plausibility that lower-crustal hydration significantly contributed to surface uplift of the latter. Density models integrating shear-wave velocity, gravity, topography, and heat flow suggest that the Colorado Plateau lower crust from 50–20 km depth is 0.055–0.106 g cm^{-3} less dense than that beneath the Great Plains ~1000 km to the east, where the surface elevation is ~1.6 km lower (Levandowski et al., 2018). This density contrast is interpreted to primarily reflect metasomatic retrogression from 40–20 km beneath the Colorado Plateau and supports ~0.9 km of isostatic surface uplift relative to the eastern Great Plains, in addition to 0.3 km surface uplift due to post-basin-subsidence rebound and 0.4 km surface uplift due to lithospheric removal. Another example highlights positive correlations among elevation, lower-crustal P-wave velocities, abundance of hydrated minerals in lower-crustal xenoliths, and their density variation (up to 0.29 g cm^{-3}) along a north–south transect through Montana, Wyoming, and Colorado (Jones et al., 2015). Taken together, these observations suggest that the isostatic effects of hydration-driven density variations within the 20 km-thick lower crust beneath the Rocky Mountains may contribute up to ~2 km to their elevation relative to the north end of the transect in Montana, where the lower crust is not hydrated. A similar correspondence of observations for the Colorado Plateau suggests that lower-crustal hydration contributes to its high surface elevation. Finally, a 0.07 g cm^{-3} contrast between the calculated densities for an altered garnet amphibolite xenolith from the Colorado Plateau and its reconstructed peak assemblage predicts ~0.4 km surface uplift for a 20 km-thick layer (Butcher et al., 2017).

5.2.2 | Additional mechanisms for uplift of anorogenic plateau

Although we have focused on the effects of metasomatic fluid–rock interactions in this study, it is well known that hydration-induced de-densification is just one of many possible mechanisms that can cause uplift in anorogenic environments. Assuming static relative positions of the subducting Farallon slab and the Colorado Plateau during the Cretaceous–Cenozoic, the linear source of aqueous fluids in our model (Figure 1a) may be expected to influence a rectangular, ~220 km (across-strike) × ~ 500 km (along-strike) horizontal region of overlying continental crust (Figure 2). However, the roughly equant ~500–700 km width of the Colorado Plateau suggests that its buoyancy derives from a point-like source. One hypothesis invokes plume-like upwelling of asthenospheric mantle, which upon impingement with the base of the plateau lithosphere would have imparted vertical stresses that contributed to its broad, centralized buoyancy (Moucha et al., 2009). Mantle upwelling may have alternatively focused along the plateau margins, but in any case is estimated to have driven a total of 15%–50% of plateau uplift since the Cretaceous (Afonso et al., 2016; Karlstrom et al., 2012; Moucha et al., 2009). Potential lithospheric buoyancy sources with a broad, horizontally centralized geometry include thermal expansion of the plateau lithosphere from basal heating and removal of the plateau mantle lithosphere by drip-like foundering (Levander et al., 2011; Moucha et al., 2009; Roy et al., 2009). Alternative mechanisms for partial removal of the plateau sub-continental lithospheric mantle (SCLM) include sheet-like delamination or tectonic bulldozing by the low-angle, eastward-subducting Farallon plate (Bird, 1984; Hernández-Uribe & Palin, 2019a; Spencer, 1996; Zandt & Ammon, 1995). Modulation of the shallower plateau lithosphere via mid-crustal flow or surface denudation may also have contributed to its buoyancy (Lazear et al., 2013; McQuarrie & Chase, 2000).

It is difficult and beyond the scope of this study to rank these mechanisms in terms of their importance, and we do not attempt to quantitatively assign an estimate of their contribution to the total documented uplift of the plateau. The difficulty of this task is exacerbated by the asynchronous nature of the documented processes and effects; for example, isostatic rebound in response to shearing away of the plateau sub-continental lithospheric mantle must necessarily follow indentation of the Farallon slab into the lithospheric root (Hernández-Uribe & Palin, 2019a). However, dehydration of the slab and the infiltration of free fluid into the overlying mantle and lower crust would have been ongoing before indentation, weakening it (Spencer, 1996).

5.3 | Limitations and caveats

Although our chosen model setup conditions and physical parameters provide a realistic representation of typical continental crust, our modelling has several limitations and caveats that represent notes of caution and opportunities for future investigation.

Firstly, our model results represent maximum estimates of hydration-induced isostatic surface uplift due to the assumption of 100%-efficient water–rock interaction concentrated in the lower, metabasic crust where density-contrast effects are most significant (Figures 4e and 5f). However, our idealized, upward-propagating hydration fronts require a percolating style of fluid flow that does not always occur in nature. Investigations of exhumed subduction-zone rocks suggest that fluid transfer in the lower crust is channelized and episodic, which implies that ascending aqueous fluids may effectively bypass much of the lower crust, travelling upwards through spatially restricted channels before 'spreading out' at shallower crustal depths where porosity is higher, initiating upward-propagating hydration fronts there instead of at the Moho (Angiboust & Raimondo, 2022; Taetz et al., 2018). For example, if ascending aqueous fluids bypass the lowermost 10 km of our composite crust via channelized flow, the ~0.7 km of isostatic surface uplift estimated for hydration of that metabasic depth range will not occur (Figure 8f). The upward-propagating hydration front would instead be most effective at depths shallower than 30 km and percolate through the upper 3 km of metabasic crust, likely all of the granodioritic crust from 27–20 km (due to its low hydration potential), and some or all of the metapelitic crust from 20–12 km (due to its high hydration potential). Using the results for the corresponding depth ranges from our closed-system models, minimal hydration of the lower–middle crust from 30–12 km is estimated to produce ~0.6 km of isostatic uplift (0.24 km for 3 km of metabasite + 0.10 km for 7 km of granodiorite + 0.24 km for 8 km of metapelite; Figure 4b,d,f).

Secondly, it has been argued that much of Earth's lower continental crust may comprise intermediate–felsic rocks rather than metabasic rocks, implying lower magnitudes of hydration-induced surface uplift in regions with non-retrogressed, granulitic lower crust (Hacker et al., 2015). This is especially true for Archean terranes, where field studies have shown that tonalite-trondhjemite-granodiorite (TTG) gneisses dominate over metabasic lithologies at middle and lower crustal depths (e.g., Condie & Kröner, 2013; Feisel et al., 2018). Using the 40–14 km depth range of our open-system, hydrated granodiorite model as a proxy for a global average of post-Archean, lower-crustal granulites imply ~0.2 km of isostatic surface uplift for a fluid-infiltration magnitude of $Q = 0.7$ (Figure 7d; Dataset S4) (Hacker et al., 2011; Rudnick & Presper, 1990). This is probably a minimum estimate because average lower-crustal granulites have more FeO (2.3 wt%) and MgO (0.8 wt%) than our modelled granodiorite, which upon hydration would stabilize greater abundances of hydrous mafic minerals (e.g., amphibole and biotite), thereby promoting greater de-densification and isostatic uplift. This point exemplifies the need to assign representative bulk compositions to any case study of interest.

Thirdly, we deliberately neglect the effect of mantle-lithosphere hydration in this study. Aqueous fluids released from subducting, devolatilizing oceanic lithosphere must pass through the overlying mantle wedge on their upward journey into the crust, and much of the ascending fluid will interact with the mantle lithosphere, both increasing lithospheric buoyancy and reducing the quantity of fluid available to hydrate the crust (Wada et al., 2012). Although this process is important, the focus of our work is to quantify the effects of crustal hydration, which has been studied to a far lesser degree than the mantle. The values of Q used in this work encompass a full spectrum of fluid-expulsion magnitudes from devolatilizing subducted slabs in modern-day subduction zones (Appendix A). We are not aware of studies that have constrained the proportion of fluid lost from a slab that is ultimately incorporated into the mantle versus overlying crust, which likely varies worldwide due to factors including slab-dip angle, convergence velocity, and thermal structure (Kirby et al., 1996). However, the existence of retrogressed (pre-eruption) lower and middle crustal xenoliths within diatremes across the Colorado Plateau demonstrates that aqueous fluids were transported into this portion of the lithospheric column during subduction of the Farallon slab, which supports the basis for our modelling (Butcher et al., 2017). Our conclusion that up to 1 km of surface uplift can be assigned to hydration of lower crust focuses solely on this process—hydration of the continental crust. Additional uplift caused by hydration of the underlying mantle is also expected to occur but has not been explored in this study.

Finally, the >500 km, SW–NE length of the Colorado plateau is more than twice the ~220 km length (strike-perpendicular) of hydrated crust in our models (Figure 2). The minimally deformed nature of the Colorado Plateau supports the expectation of a roughly consistent horizontal geometry throughout the late Cretaceous–middle Cenozoic, when the Farallon slab subducted beneath it towards the NE. Following our model subduction geometry (Figure 1a), a 500 km length of hydrated crust overlies a ~9°-dipping subducting slab. Assuming the same fluid-loss magnitude ($dq'dx_{z\,=\,40\text{–}120\text{ km}}$) as that for the 20°-dipping Cascadia slab implies a reduction of the bulk-average fluid-infiltration magnitude ($dq'dx/dy$) to less than half of our modelled value. Our models presume steady-state subduction and fluid-supply rate, which does not likely characterize subduction over million-year timescales. Secular variation in the angle, velocity, age, and sedimentary-layer thickness of dynamically subducting oceanic lithosphere implies a likely variation of fluid supply and flux throughout the life cycle of a subduction zone.

5.4 | Applicability to other plateaus worldwide

Although our modelling focuses on uplift of the Colorado Plateau, the results are generalizable to any continental crust that experiences fluid infiltration at its base, assuming similar bulk compositions and metamorphic grades. The greatest crustal fluid-flux magnitudes are expected to occur above low-angle-subducting slabs, which themselves underlie the thinnest columns of asthenospheric mantle through which expelled fluids must pass before entering the lithosphere. In special cases of lithospheric mantle removal, which has been proposed by some researchers for the Colorado Plateau, fluid may infiltrate more or less directly into the lower crust. Low-angle subduction on Earth today occurs for subduction of buoyant oceanic crust, which can derive its buoyancy from the occurrence of aseismic ridges, oceanic plateaus, and/or seamounts (Gutscher et al., 2000). For example, the dip angle is known to vary for subducting oceanic lithosphere along the western coast of South America, with low-angle subduction of the Peruvian and the Pampean (Chilean) slabs being spatially correlated with subduction of the Nazca Ridge and the Juan Fernandéz Ridge, respectively, which represent bathymetric highs (Antonijevic et al., 2015; Ramos & Folguera, 2009). This phenomenon has been linked to formation of the Altiplano–Puna plateau, which is located in Bolivia, Peru, and Chile and provides a well-documented example of a high-elevation orogenic plateau in a non-collisional tectonic setting (Gianni et al., 2020). To our knowledge, there has been no focused study of whether dehydration of the underthrust Peruvian/Pampean slabs has influenced surface uplift in this area, as accepted explanations for formation of the southern Puna plateau involve focused intraplate contraction in the Southern Central Andes between latitudes 35°S and 38°S, driven by a strong mechanical coupling between both plates (Allmendinger et al., 1997; Ramos et al., 2002). Interestingly, Kay et al. (1994) also documented petrological evidence for lithospheric delamination beneath the Argentinian portion of the Puna plateau, drawing an analogy to lithospheric loss beneath the Colorado Plateau (Li et al., 2008). We therefore consider it an interesting opportunity for future study to apply the modelling documented in this work to examine the impact on surface uplift of the Altiplano-Puna plateau of South America.

The Tibet Plateau is another well-studied plateau on Earth and shares many morphological similarities with the Colorado Plateau, although it is not anorogenic given its close spatial and temporal association with the formation of the Himalaya Mountains as a result of the Cenozoic India-Asia collision (Kapp & DeCelles, 2019; Royden et al., 2008; Searle et al., 2011). Several regional-scale geophysical surveys of the Himalaya–Tibet region reveal low-angle underthrusting of Indian lower crust beneath Tibet (Nabelek et al., 2009; Owens & Zandt, 1997; Tilmann et al., 2003). However, the lithological character of the Tibet Plateau lower crust is likely dissimilar to that of the Colorado Plateau, rendering direct comparison of estimated uplift in this study to Tibet of little practical use. In particular, due to the nature of the southern Asian margin—the Lhasa Terrane—during closure of the Neo-Tethys ocean being an active continental magmatic arc, akin to the Andes today, the lower crust of Tibet prior to the onset of collision would have been notably higher-grade than that of the anorogenic lower crust of the Colorado Plateau. Petrological investigation of xenoliths and exhumed portions of lower crust in southeast Tibet indicate ambient upper-amphibolite-facies to high-pressure-granulite-facies conditions (e.g., Palin et al., 2014; Zhang et al., 2020, 2022). As such, the effects of fluid infiltration by dehydration and devolatilization of subducted Indian oceanic and/or continental crust are more likely to resemble the nominally anhydrous end member of our modelling, given the dry nature of granulite facies rocks (Newton et al., 2014). Akin to the Altiplano, we are unaware of studies that have focused explicitly on the effect of lower crustal hydration on surface uplift.

One final point of note related to the application of our modelling work to alternative geological settings outside of North America should mention the accepted prevalence of low-angle subduction during the Archean (Hunen & Moyen, 2012). Due to higher mantle potential temperatures within the early Earth, thicker and more-mafic oceanic lithosphere is expected to have been notably more buoyant than its modern-day equivalent (Herzberg et al., 2010; Palin & White, 2016). Shallow-angle subduction and the thinning of an intermediate mantle wedge at convergent margins has been championed to explain some geochemical characteristics of earth's earliest felsic crust, and thus, it is expected that the underthrusting of hydrated oceanic lithosphere beneath proto-continents would result in similar fluid–rock interactions as documented here in our modelling study of the Colorado Plateau (Martin et al., 2005). However, alongside differences in the composition of both oceanic crust and equivalent continental counterparts during the Archean compared with the modern day, higher thermal gradients in arcs mean that the xenolith-derived P–T gradients utilized to represent stable, anorogenic crust in intraplate environments for the Phanerozoic allow no direct comparison with active plate margins, whether on the modern Earth or during the Precambrian (Korenaga, 2006; Palin et al., 2021; Tang et al., 2016). This again represents a valuable potential direction for future research in this field.

6 | CONCLUSIONS

Oceanic lithosphere that subducts at low angles beneath continental margins transports and releases significant masses of aqueous fluids that percolate into, metasomatize, and de-densify continental interiors. We use open-system, reactive-transport petrological modelling to interrogate the potential for basal H_2O fluid infiltration into lower–middle continental crust to hydrate and de-densify nominally anhydrous metabasite, granodiorite, and metapelite lithologies, thereby driving anorogenic plateau uplift. Lower-crustal metabasite, when subjected to H_2O fluid infiltration of 0.8×10^6 kg m^{-2}, hydrates up to 3.0 wt% H_2O and de-densifies up to 10% from 40 to 26 km depth, predicting ~1 km isostatic surface uplift under favourable conditions. Granodiorite and metapelite, by comparison, predict less surface uplift (~0.3 km) due to trivial de-densification of the former (up to 1.8%) across the lower–middle crust (40–17 km depth) and moderate de-densification of the latter (up to 4.3%) across a narrow depth range of the lower crust (40–31 km depth). A composite-crust model comprising metabasite, granodiorite, and metapelite in order of decreasing depth closely resembles the metabasite model crust.

Previously published thermo-kinematic and petrological modelling results of H_2O fluid loss from the modern, 20°-dipping Cascadia slab at 40–120 km depth suggest a maximum H_2O fluid flux of 0.05×10^6 kg m^{-2} Myr^{-1} into the overlying Moho. Integrating our modelling results with an interpretation of the modern Cascadia subduction zone as an analogue to subduction and dewatering of the ancient Farallon slab beneath the Colorado proto-Plateau during the Cenozoic suggests that hydration of its mafic lower crust over 16 Myr could have driven up to ~1 km of the net ~2 km surface uplift that it has undergone since the late Cretaceous, although this value represents a maximum assuming perfect efficiency of both fluid infiltration and reaction.

ACKNOWLEDGEMENTS

The authors acknowledge support from NSF grant EAR-1926134 awarded to RMP and EJC. We thank Peter van Keken, Geoff Abers, and Cian Wilson for providing updated model data and insightful discussion. We thank two anonymous reviewers and handling editor Katy Evans for a series of helpful and insightful comments that led to significant improvements of the manuscript during the revision stage.

ORCID

James R. Worthington https://orcid.org/0000-0002-1442-8265

REFERENCES

Abers, G. A., van Keken, P. E., & Wilson, C. R. (2020). Deep decoupling in subduction zones: Observations and temperature limits. *Geosphere*, *16*, 1408–1424. https://doi.org/10.1130/GES02278.1

Afonso, J. C., Rawlinson, N., Yang, Y., Schutt, D. L., Jones, A. G., Fullea, J., & Griffin, W. L. (2016). 3-D multiobservable probabilistic inversion for the compositional and thermal structure of the lithosphere and upper mantle: III. Thermochemical tomography in the Western-Central U.S. *Journal of Geophysical Research: Solid Earth*, *121*, 7337–7370. https://doi.org/10.1002/2016JB013049

Ague, J. J. (1991). Evidence for major mass transfer and volume strain during regional metamorphism of pelites. *Geology*, *19*, 855–858. https://doi.org/10.1130/0091-7613(1991)019<0855:EFMMTA>2.3.CO;2

Allmendinger, R. W., Jordan, T. E., Kay, S. M., & Isacks, B. L. (1997). The evolution of the Altiplano-Puna plateau of the Central Andes. *Annual Review of Earth and Planetary Sciences*, *25*, 139–174. https://doi.org/10.1146/annurev.earth.25.1.139

Angiboust, S., & Raimondo, T. (2022). Permeability of subducted oceanic crust revealed by eclogite-facies vugs. *Geology*, *50*, 964–968. https://doi.org/10.1130/G50066.1

Antonijevic, S. K., Wagner, L. S., Kumar, A., Beck, S. L., Long, M. D., Zandt, G., Tavera, H., & Condori, C. (2015). The role of ridges in the formation and longevity of flat slabs. *Nature*, *524*, 212–215. https://doi.org/10.1038/nature14648

Atwater, T. (1970). Implications of plate tectonics for the Cenozoic tectonic evolution of Western North America. *GSA Bulletin*, *81*, 3513–3536. https://doi.org/10.1130/0016-7606(1970)81[3513:IOPTFT]2.0.CO;2

Behr, W. M., & Smith, D. (2016). Deformation in the mantle wedge associated with Laramide flat-slab subduction. *Geochemistry, Geophysics, Geosystems*, *17*, 2643–2660. https://doi.org/10.1002/2016GC006361

Bird, P. (1979). Continental delamination and the Colorado Plateau. *Journal of Geophysical Research*, *84*, 7561–7571. https://doi.org/10.1029/JB084iB13p07561

Bird, P. (1984). Laramide crustal thickening event in the Rocky Mountain Foreland and Great Plains. *Tectonics*, *3*, 741–758. https://doi.org/10.1029/TC003i007p00741

Bird, P. (1988). Formation of the Rocky Mountains, Western United States: A continuum computer model. *Science*, *239*, 1501–1507. https://doi.org/10.1126/science.239.4847.1501

Braun, J., & Beaumont, C. (1989). A physical explanation of the relation between flank uplifts and the breakup unconformity at rifted continental margins. *Geology*, *17*, 760–764. https://doi.org/10.1130/0091-7613(1989)017<0760:APEOTR>2.3.CO;2

Butcher, L. A., Mahan, K. H., & Allaz, J. M. (2017). Late Cretaceous crustal hydration in the Colorado Plateau, USA, from xenolith petrology and monazite geochronology. *Lithosphere*, *9*, 561–578. https://doi.org/10.1130/L583.1

Chapman, D. S. (1986). Thermal gradients in the continental crust. *Geological Society, London, Special Publications*, *24*, 63–70. https://doi.org/10.1144/GSL.SP.1986.024.01.07

Chin, E. J., Chilson-Parks, B., Boneh, Y., Hirth, G., Saal, A. E., Hearn, B. C., & Hauri, E. H. (2021). The peridotite deformation cycle in cratons and the deep impact of subduction. *Tectonophysics*, *817*, 229029. https://doi.org/10.1016/j.tecto.2021.229029

Condie, K. C. (1982). Plate-tectonics model for Proterozoic continental accretion in the southwestern United States. *Geology*, *10*, 37–42. https://doi.org/10.1130/0091-7613(1982)10<37:PMFPCA>2.0.CO;2

Condie, K. C., & Kröner, A. (2013). The building blocks of continental crust: Evidence for a major change in the tectonic setting of continental growth at the end of the Archean. *Gondwana Research*, *23*, 394–402. https://doi.org/10.1016/j.gr.2011.09.011

Condie, K. C., & Selverstone, J. (1999). The crust of the Colorado Plateau: New views of an old arc. *The Journal of Geology*, *107*, 387–397. https://doi.org/10.1086/314363

Coney, P. J., & Reynolds, S. J. (1977). Cordilleran Benioff zones. *Nature*, *270*, 403–406. https://doi.org/10.1038/270403a0

Connolly, J. A. D. (2005). Computation of phase equilibria by linear programming: A tool for geodynamic modeling and its application to subduction zone decarbonation. *Earth and Planetary Science Letters*, *236*, 524–541. https://doi.org/10.1016/j.epsl.2005.04.033

Connolly, J. A. D., & Petrini, K. (2002). An automated strategy for calculation of phase diagram sections and retrieval of rock properties as a function of physical conditions. *Journal of Metamorphic Geology*, *20*, 697–708. https://doi.org/10.1046/j.1525-1314.2002.00398.x

Dickinson, W. R., Snyder, W. S., & Matthews, V. III (1978). *Plate tectonics of the Laramide orogeny, Laramide folding associated with basement block faulting in the Western United States*. Geological Society of America, p. 0. https://doi.org/10.1130/MEM151-p355

Ebinger, C. J., Bechtel, T. D., Forsyth, D. W., & Bowin, C. O. (1989). Effective elastic plate thickness beneath the East African and Afar plateaus and dynamic compensation of the uplifts. *Journal of Geophysical Research: Solid Earth*, *94*, 2883–2901. https://doi.org/10.1029/JB094iB03p02883

Etheridge, M. A., Wall, V. J., & Vernon, R. H. (1983). The role of the fluid phase during regional metamorphism and deformation. *Journal of Metamorphic Geology*, *1*, 205–226. https://doi.org/10.1111/j.1525-1314.1983.tb00272.x

Feisel, Y., White, R. W., Palin, R. M., & Johnson, T. E. (2018). New constraints on granulite facies metamorphism and melt production in the Lewisian Complex, Northwest Scotland. *Journal of Metamorphic Geology*, *36*, 799–819. https://doi.org/10.1111/jmg.12311

Flowers, R. M. (2010). The enigmatic rise of the Colorado Plateau. *Geology*, *38*, 671–672. https://doi.org/10.1130/focus072010.1

Flowers, R. M., Wernicke, B. P., & Farley, K. A. (2008). Unroofing, incision, and uplift history of the southwestern Colorado Plateau from apatite (U-Th)/He thermochronometry. *GSA Bulletin*, *120*, 571–587. https://doi.org/10.1130/B26231.1

Gianni, G. M., García, H. P. A., Pesce, A., Lupari, M., González, M., & Giambiagi, L. (2020). Oligocene to present shallow subduction beneath the southern Puna plateau. *Tectonophysics*, *780*, 228402. https://doi.org/10.1016/j.tecto.2020.228402

Green, E., Holland, T., & Powell, R. (2007). An order-disorder model for omphacitic pyroxenes in the system jadeite-diopside-hedenbergite-acmite, with applications to eclogitic rocks. *American Mineralogist*, *92*, 1181–1189. https://doi.org/10.2138/am.2007.2401

Green, E. C. R., White, R. W., Diener, J. F. A., Powell, R., Holland, T. J. B., & Palin, R. M. (2016). Activity–composition relations for the calculation of partial melting equilibria in metabasic rocks. *Journal of Metamorphic Geology*, *34*, 845–869. https://doi.org/10.1111/jmg.12211

Grove, M., Lovera, O., Harrison, M., Johnson, S. E., Paterson, S. R., Fletcher, J. M., Girty, G. H., Kimbrough, D. L., & Martín-Barajas, A. (2003). Late Cretaceous cooling of the east-central Peninsular Ranges Batholith (33 degrees N); relationship to La Posta Pluton emplacement, Laramide shallow subduction, and forearc sedimentation, Tectonic evolution of northwestern Mexico and the southwestern USA. Geological Society of America, p. 0, https://doi.org/10.1130/0-8137-2374-4.355

Guiraud, M., Powell, R., & Rebay, G. (2001). H2O in metamorphism and unexpected behaviour in the preservation of metamorphic mineral assemblages. *Journal of Metamorphic Geology*, *19*, 445–454. https://doi.org/10.1046/j.0263-4929.2001.00320.x

Gutscher, M. A., Spakman, W., Bijwaard, H., & Engdahl, E. R. (2000). Geodynamics of flat subduction: Seismicity and tomographic constraints from the Andean margin. *Tectonics*, *19*, 814–833. https://doi.org/10.1029/1999TC001152

Hacker, B. R., Kelemen, P. B., & Behn, M. D. (2011). Differentiation of the continental crust by relamination. *Earth and Planetary Science Letters*, *307*, 501–516. https://doi.org/10.1016/j.epsl.2011.05.024

Hacker, B. R., Kelemen, P. B., & Behn, M. D. (2015). Continental lower crust. *Annual Review of Earth and Planetary Sciences*, *43*, 167–205. https://doi.org/10.1146/annurev-earth-050212-124117

Hanson, R. B. (1992). Effects of fluid production on fluid flow during regional and contact metamorphism. *Journal of Metamorphic Geology*, *10*, 87–97. https://doi.org/10.1111/j.1525-1314.1992.tb00073.x

Helmstaedt, H. H., & Schulze, D. J. (1991). Early to mid-tertiary inverted metamorphic gradient under the Colorado Plateau: Evidence from eclogite xenoliths in ultramafic microbreccias, Navajo volcanic field. *Journal of Geophysical Research: Solid Earth*, *96*, 13225–13235. https://doi.org/10.1029/91JB00284

Hernández-Uribe, D., & Palin, R. M. (2019a). Catastrophic shear-removal of subcontinental lithospheric mantle beneath the Colorado Plateau by the subducted Farallon slab. *Scientific Reports*, *9*, 8153. https://doi.org/10.1038/s41598-019-44628-y

Hernández-Uribe, D., & Palin, R. M. (2019b). A revised petrological model for subducted oceanic crust: Insights from phase equilibrium modelling. *Journal of Metamorphic Geology*, *37*, 745–768. https://doi.org/10.1111/jmg.12483

Herzberg, C., Condie, K., & Korenaga, J. (2010). Thermal history of the Earth and its petrological expression. *Earth and Planetary Science Letters*, *292*, 79–88. https://doi.org/10.1016/j.epsl.2010.01.022

Holland, T., & Powell, R. (2003). Activity–composition relations for phases in petrological calculations: An asymmetric multicomponent formulation. *Contributions to Mineralogy and Petrology*, *145*, 492–501. https://doi.org/10.1007/s00410-003-0464-z

Holland, T. J. B., & Powell, R. (2011). An improved and extended internally consistent thermodynamic dataset for phases of petrological interest, involving a new equation of state for solids. *Journal of Metamorphic Geology*, *29*, 333–383. https://doi.org/10.1111/j.1525-1314.2010.00923.x

Humphreys, E., Hessler, E., Dueker, K., Farmer, G. L., Erslev, E., & Atwater, T. (2003). How Laramide-age Hydration of North American lithosphere by the Farallon slab controlled subsequent activity in the Western United States. *International Geology Review*, *45*, 575–595. https://doi.org/10.2747/0020-6814.45.7.575

Humphreys, E. D., Schmandt, B., Bezada, M. J., & Perry-Houts, J. (2015). Recent craton growth by slab stacking beneath Wyoming. *Earth and Planetary Science Letters*, *429*, 170–180. https://doi.org/10.1016/j.epsl.2015.07.066

Hunen, J. V., & Moyen, J.-F. (2012). Archean subduction: Fact or fiction? *Annual Review of Earth and Planetary Sciences*, *40*, 195–219. https://doi.org/10.1146/annurev-earth-042711-105255

Huntington, K. W., Wernicke, B. P., & Eiler, J. M. (2010). Influence of climate change and uplift on Colorado Plateau paleotemperatures from carbonate clumped isotope thermometry. *Tectonics*, *29*, TC3005. https://doi.org/10.1029/2009TC002449

Jones, C. H., Mahan, K. H., Butcher, L. A., Levandowski, W. B., & Farmer, G. L. (2015). Continental uplift through crustal hydration. *Geology*, *43*, 355–358. https://doi.org/10.1130/G36509.1

Kapp, P., & DeCelles, P. G. (2019). Mesozoic–Cenozoic geological evolution of the Himalayan-Tibetan orogen and working tectonic hypotheses. *American Journal of Science*, *319*, 159–254. https://doi.org/10.2475/03.2019.01

Karlstrom, K. E., Coblentz, D., Dueker, K., Ouimet, W., Kirby, E., Van Wijk, J., Schmandt, B., Kelley, S., Lazear, G., Crossey, L. J., Crow, R., Aslan, A., Darling, A., Aster, R., MacCarthy, J., Hansen, S. M., Stachnik, J., Stockli, D. F., Garcia, R. V., … Group, a.t.C.W. (2012). Mantle-driven dynamic uplift of the Rocky Mountains and Colorado Plateau and its surface response: Toward a unified hypothesis. *Lithosphere*, *4*, 3–22. https://doi.org/10.1130/L150.1

Kay, S. M., Coira, B., & Viramonte, J. (1994). Young mafic back arc volcanic-rocks as indicators of continental lithospheric delamination beneath the argentine Puna plateau, Central Andes. *Journal of Geophysical Research-Solid Earth*, *99*, 24323–24339. https://doi.org/10.1029/94JB00896

Kerrick, D. M., & Connolly, J. A. D. (2001). Metamorphic devolatilization of subducted marine sediments and the transport of volatiles into the Earth's mantle. *Nature*, *411*, 293–296. https://doi.org/10.1038/35077056

Kirby, S. H., Stein, S., Okal, E. A., & Rubie, D. C. (1996). Metastable mantle phase transformations and deep earthquakes in subducting oceanic lithosphere. *Reviews of Geophysics*, *34*, 261–306. https://doi.org/10.1029/96RG01050

Korenaga, J. (2006). Archean geodynamics and the thermal evolution of earth. *Archean Geodynamics and Environments*, *164*, 7–32. https://doi.org/10.1029/164GM03

Lazear, G., Karlstrom, K., Aslan, A., & Kelley, S. (2013). Denudation and flexural isostatic response of the Colorado Plateau and southern Rocky Mountains region since 10 ma. *Geosphere*, *9*, 792–814. https://doi.org/10.1130/GES00836.1

Le Maitre, R. W. (1976). The chemical variability of some common igneous rocks. *Journal of Petrology*, *17*, 589–598. https://doi.org/10.1093/petrology/17.4.589

Lee, C.-T. A., Luffi, P., & Chin, E. J. (2011). Building and destroying continental mantle. *Annual Review of Earth and Planetary Sciences*, *39*, 59–90. https://doi.org/10.1146/annurev-earth-040610-133505

Levander, A., Schmandt, B., Miller, M. S., Liu, K., Karlstrom, K. E., Crow, R. S., Lee, C. T. A., & Humphreys, E. D. (2011). Continuing Colorado plateau uplift by delamination-style convective lithospheric downwelling. *Nature*, *472*, 461–465. https://doi.org/10.1038/nature10001

Levandowski, W., Jones, C. H., Butcher, L. A., & Mahan, K. H. (2018). Lithospheric density models reveal evidence for Cenozoic uplift of the Colorado Plateau and Great Plains by lower-crustal hydration. *Geosphere*, *14*, 1150–1164. https://doi.org/10.1130/GES01619.1

Li, Z.-X. A., Lee, C.-T. A., Peslier, A. H., Lenardic, A., & Mackwell, S. J. (2008). Water contents in mantle xenoliths from the Colorado Plateau and vicinity: Implications for the mantle rheology and hydration-induced thinning of continental lithosphere. *Journal of Geophysical Research: Solid Earth*, *113*, B09210. https://doi.org/10.1029/2007JB005540

Liu, L., Gurnis, M., Seton, M., Saleeby, J., Müller, R. D., & Jackson, J. M. (2010). The role of oceanic plateau subduction in the Laramide orogeny. *Nature Geoscience*, *3*, 353–357. https://doi.org/10.1038/ngeo829

Martin, H., Smithies, R. H., Rapp, R., Moyen, J. F., & Champion, D. (2005). An overview of adakite, tonalite–trondhjemite–granodiorite (TTG), and sanukitoid: Relationships and some implications for crustal evolution. *Lithos*, *79*, 1–24. https://doi.org/10.1016/j.lithos.2004.04.048

McKenzie, D. P., & Parker, R. L. (1967). The North Pacific: An example of tectonics on a sphere. *Nature*, *216*, 1276–1280. https://doi.org/10.1038/2161276a0

McQuarrie, N., & Chase, C. G. (2000). Raising the Colorado Plateau. *Geology*, *28*, 91–94. https://doi.org/10.1130/0091-7613(2000)028<0091:RTCP>2.0.CO;2

Molnar, P. (1988). Continental tectonics in the aftermath of plate tectonics. *Nature*, *335*, 131–137. https://doi.org/10.1038/335131a0

Moucha, R., Forte, A. M., Rowley, D. B., Mitrovica, J. X., Simmons, N. A., & Grand, S. P. (2009). Deep mantle forces and the uplift of the Colorado Plateau. *Geophysical Research Letters*, *36*, L19310. https://doi.org/10.1029/2009GL039778

Nabelek, J., Hetenyi, G., Vergne, J., Sapkota, S., Kafle, B., Jiang, M., Su, H. P., Chen, J., Huang, B. S., & Hi, C. T. (2009). Underplating in the Himalaya-Tibet collision zone revealed by the Hi-CLIMB experiment. *Science*, *325*, 1371–1374. https://doi.org/10.1126/science.1167719

Newton, R. C., Touret, J. L. R., & Aranovich, L. Y. (2014). Fluids and H2O activity at the onset of granulite facies metamorphism. *Precambrian Research*, *253*, 17–25. https://doi.org/10.1016/j.precamres.2014.06.009

Owens, T. J., & Zandt, G. (1997). Implications of crustal property variations for models of Tibetan plateau evolution. *Nature*, *387*, 37–43. https://doi.org/10.1038/387037a0

Palin, R. M., Moore, J. D. P., Zhang, Z., Huang, G., Wade, J., & Dyck, B. (2021). Mafic Archean continental crust prohibited exhumation of orogenic UHP eclogite. *Geoscience Frontiers*, *12*, 101225. https://doi.org/10.1016/j.gsf.2021.101225

Palin, R. M., Searle, M. P., St-Onge, M. R., Waters, D. J., Roberts, N. M. W., Horstwood, M. S. A., Parrish, R. R., Weller, O. M., Chen, S., & Yang, J. (2014). Monazite geochronology and petrology of kyanite- and sillimanite-grade migmatites from the northwestern flank of the eastern Himalayan syntaxis. *Gondwana Research*, *26*, 323–347. https://doi.org/10.1016/j.gr.2013.06.022

Palin, R. M., & White, R. W. (2016). Emergence of blueschists on Earth linked to secular changes in oceanic crust composition. *Nature Geoscience*, *9*, 60–64. https://doi.org/10.1038/ngeo2605

Parsons, T., & McCarthy, J. (1995). The active southwest margin of the Colorado Plateau: Uplift of mantle origin. *GSA Bulletin*, *107*, 139–147. https://doi.org/10.1130/0016-7606(1995)107<0139:TASMOT>2.3.CO;2

Peacock, S. A. (1990). Fluid processes in subduction zones. *Science*, *248*, 329–337. https://doi.org/10.1126/science.248.4953.329

Porter, R., Hoisch, T., & Holt, W. E. (2017). The role of lower-crustal hydration in the tectonic evolution of the Colorado Plateau. *Tectonophysics*, *712-713*, 221–231. https://doi.org/10.1016/j.tecto.2017.05.025

Ramos, V., Cristallini, E., & Perez, E. (2002). The Pampean flat-slab of the Central Andes: Journal of South American Earth Science, v. 15. *Journal of South American Earth Sciences*, *15*, 59–78. https://doi.org/10.1016/S0895-9811(02)00006-8

Ramos, V. A., & Folguera, A. (2009). Andean flat-slab subduction through time. *Geological Society, London, Special Publications*, *327*, 31–54. https://doi.org/10.1144/SP327.3

Roberts, G. G., White, N. J., Martin-Brandis, G. L., & Crosby, A. G. (2012). An uplift history of the Colorado Plateau and its surroundings from inverse modeling of longitudinal river profiles. *Tectonics*, *31*, TC4022. https://doi.org/10.1029/2012TC003107

Roy, M., Jordan, T. H., & Pederson, J. (2009). Colorado Plateau magmatism and uplift by warming of heterogeneous lithosphere. *Nature*, *459*, 978–982. https://doi.org/10.1038/nature08052

Roy, M., MacCarthy, J. K., & Selverstone, J. (2005). *Upper mantle structure beneath the eastern Colorado Plateau and Rio Grande rift revealed by Bouguer gravity, seismic velocities, and xenolith data* (Vol. 6, p. 6). Geochemistry. https://doi.org/10.1029/2005GC001008

Royden, L. H., Burchfiel, B. C., & van der Hilst, R. D. (2008). The geological evolution of the Tibetan plateau. *Science*, *321*, 1054–1058. https://doi.org/10.1126/science.1155371

Rudnick, R., & Presper, T. (1990). Geochemistry of intermediate/-to high-pressure granulites. In *Granulites and Crustal Evolution*, NATO ASI Series (Vol. 311, pp. 523–550). Dordrecht, Netherlands: Springer. https://doi.org/10.1007/978-94-009-2055-2_27

Rudnick, R. L., & Gao, J. (2014). The composition of the continental crust. In H. D. Holland & H. D. Turekian (Eds.), *The crust* (pp. 1–51). Elsevier-Pergamon. https://doi.org/10.1016/B978-0-08-095975-7.00301-6

Rudnick, R. L., & Gao, S. (2003). Composition of the continental crust. In H. D. Holland & K. K. Turekian (Eds.), *Treatise on geochemistry*. Elsevier-Pergamon. https://doi.org/10.1016/B0-08-043751-6/03016-4

Rudnick, R. L., McDonough, W. F., & O'Connell, R. J. (1998). Thermal structure, thickness and composition of continental lithosphere. *Chemical Geology*, *145*, 395–411. https://doi.org/10.1016/S0009-2541(97)00151-4

Sahagian, D. (1987). Epeirogeny and eustatic sea level changes as inferred from cretaceous shoreline deposits: Applications to the central and western United States. *Journal of Geophysical Research: Solid Earth*, *92*, 4895–4904. https://doi.org/10.1029/JB092iB06p04895

Sahagian, D., Proussevitch, A., & Carlson, W. (2002). Timing of Colorado Plateau uplift: Initial constraints from vesicular basalt-derived paleoelevations. *Geology*, *30*, 807–810. https://doi.org/10.1130/0091-7613(2002)030<0807:TOCPUI>2.0.CO;2

Schulze, D. J., Davis, D. W., Helmstaedt, H., & Joy, B. (2015). Timing of the Cenozoic "Great Hydration" event beneath the Colorado Plateau: Th-Pb dating of monazite in Navajo volcanic field metamorphic eclogite xenoliths. *Geology*, *43*, 727–730. https://doi.org/10.1130/G36932.1

Searle, M. P., Elliott, J. R., Phillips, R. J., & Chung, S.-L. (2011). Crustal–lithospheric structure and continental extrusion of Tibet. *Journal of the Geological Society*, *168*, 633–672. https://doi.org/10.1144/0016-76492010-139

Smith, D. (2010). Antigorite peridotite, Metaserpentinite, and other inclusions within diatremes on the Colorado Plateau, SW USA: Implications for the mantle wedge during low-angle subduction. *Journal of Petrology*, *51*, 1355–1379. https://doi.org/10.1093/petrology/egq022

Smith, D., Connelly, J. N., Manser, K., Moser, D. E., Housh, T. B., McDowell, F. W., & Mack, L. E. (2004). *Evolution of Navajo eclogites and hydration of the mantle wedge below the Colorado Plateau, southwestern United States* (Vol. 5) (p. 5). Geochemistry. https://doi.org/10.1029/2003GC000675

Spencer, J. E. (1996). Uplift of the Colorado Plateau due to lithosphere attenuation during Laramide low-angle subduction. *Journal of Geophysical Research: Solid Earth*, *101*, 13595–13609. https://doi.org/10.1029/96JB00818

Sun, W., Arculus, R. J., Kamenetsky, V. S., & Binns, R. A. (2004). Release of gold-bearing fluids in convergent margin magmas prompted by magnetite crystallization. *Nature*, *431*, 975–978. https://doi.org/10.1038/nature02972

Syracuse, E. M., van Keken, P. E., & Abers, G. A. (2010). The global range of subduction zone thermal models. *Physics of the Earth and Planetary Interiors*, *183*, 73–90. https://doi.org/10.1016/j.pepi.2010.02.004

Taetz, S., John, T., Bröcker, M., Spandler, C., & Stracke, A. (2018). Fast intraslab fluid-flow events linked to pulses of high pore fluid pressure at the subducted plate interface. *Earth and Planetary Science Letters*, *482*, 33–43. https://doi.org/10.1016/j.epsl.2017.10.044

Tang, M., Chen, K., & Rudnick, R. L. (2016). Archean upper crust transition from mafic to felsic marks the onset of plate tectonics. *Science*, *351*, 372–375. https://doi.org/10.1126/science.aad5513

Thompson, G. A., & Zoback, M. L. (1979). Regional geophysics of the Colorado Plateau. *Tectonophysics*, *61*, 149–181. https://doi.org/10.1016/0040-1951(79)90296-8

Tilmann, F., Ni, J., & Team, I. I. S. (2003). Seismic imaging of the downwelling Indian lithosphere beneath Central Tibet. *Science*, *300*, 1424–1427. https://doi.org/10.1126/science.1082777

Turcotte, D. L., & Schubert, G. (2002). *Geodynamics*. Cambridge University Press. https://doi.org/10.1017/CBO9780511807442

Usui, T., Nakamura, E., Kobayashi, K., Maruyama, S., & Helmstaedt, H. (2003). Fate of the subducted Farallon plate inferred from eclogite xenoliths in the Colorado Plateau. *Geology*, *31*, 589–592. https://doi.org/10.1130/0091-7613(2003)031<0589:FOTSFP>2.0.CO;2

van Keken, P. E., Hacker, B. R., Syracuse, E. M., & Abers, G. A. (2011). Subduction factory: 4. Depth-dependent flux of H2O from subducting slabs worldwide. *Journal of Geophysical Research*, *116*, B01401. https://doi.org/10.1029/2010JB007922

Wada, I., Behn, M. D., & Shaw, A. M. (2012). Effects of heterogeneous hydration in the incoming plate, slab rehydration, and mantle wedge hydration on slab-derived H2O flux in subduction zones. *Earth and Planetary Science Letters*, *353-354*, 60–71. https://doi.org/10.1016/j.epsl.2012.07.025

Wade, J., Dyck, B., Palin, R. M., Moore, J. D. P., & Smye, A. J. (2017). The divergent fates of primitive hydrospheric water on Earth and Mars. *Nature*, *552*, 391–394. https://doi.org/10.1038/nature25031

Westrich, H. R., Stockman, H. W., & Eichelberger, J. C. (1988). Degassing of rhyolitic magma during ascent and emplacement. *Journal of Geophysical Research: Solid Earth*, *93*, 6503–6511. https://doi.org/10.1029/JB093iB06p06503

White, R. W., Powell, R., Holland, T. J. B., Johnson, T. E., & Green, E. C. R. (2014). New mineral activity–composition relations for thermodynamic calculations in metapelitic systems. *Journal of Metamorphic Geology*, *32*, 261–286. https://doi.org/10.1111/jmg.12071

Whitmeyer, S. J., & Karlstrom, K. E. (2007). Tectonic model for the Proterozoic growth of North America. *Geosphere*, *3*, 220–259. https://doi.org/10.1130/GES00055.1

Whitney, D. L., & Evans, B. W. (2010). Abbreviations for names of rock-forming minerals. *American Mineralogist*, *95*(1), 185–187. https://doi.org/10.2138/am.2010.3371

Wichura, H., Bousquet, R., Oberhänsli, R., Strecker, M. R., & Trauth, M. H. (2011). The Mid-Miocene East African Plateau: A pre-rift topographic model inferred from the emplacement of the phonolitic Yatta lava flow, Kenya. *Geological Society, London, Special Publications*, *357*, 285–300. https://doi.org/10.1144/SP357.15

Wolfe, J. A., Schorn, H. E., Forest, C. E., & Molnar, P. (1997). Paleobotanical evidence for high altitudes in Nevada during the Miocene. *Science*, *276*, 1672–1675. https://doi.org/10.1126/science.276.5319.1672

Yardley, B. W. D., & Bodnar, R. J. (2014). Fluids in the continental crust. *Geochemical Perspectives*, *3*, 1–2. https://doi.org/10.7185/geochempersp.3.1

Zandt, G., & Ammon, C. J. (1995). Continental-crust composition constrained by measurements of crustal Poissons ratio. *Nature*, *374*, 152–154. https://doi.org/10.1038/374152a0

Zhang, Z., Ding, H., Palin, R. M., Dong, X., Tian, Z., & Chen, Y. (2020). The lower crust of the Gangdese magmatic arc, southern Tibet, implication for the growth of continental crust. *Gondwana Research*, *77*, 136–146. https://doi.org/10.1016/j.gr.2019.07.010

Zhang, Z., Ding, H., Palin, R. M., Dong, X., Tian, Z., Kang, D., Jiang, Y., Qin, S., & Li, W. (2022). On the origin of high-pressure mafic granulite in the Eastern Himalayan Syntaxis: Implications for the tectonic evolution of the Himalayan orogen. *Gondwana Research*, *104*, 4–22. https://doi.org/10.1016/j.gr.2021.05.011

SUPPORTING INFORMATION

Additional supporting information can be found online in the Supporting Information section at the end of this article.

Dataset S1. Estimated pre-arc Moho H_2O flux from subducting oceanic lithosphere.

Dataset S2. Geotherm calculation.

Dataset S3. Perple_X closed-system data.

Dataset S4. Perple_X open-system (TITRATE) data.

How to cite this article: Worthington, J. R., Chin, E. J., & Palin, R. M. (2024). Metasomatism of the continental crust and its impact on surface uplift: Insights from reactive-transport modelling. *Journal of Metamorphic Geology*, 1–27. https://doi.org/10.1111/jmg.12772

APPENDIX A: SUBDUCTION-RELATED FLUID FLUX INTO OVERLYING CONTINENTAL LOWER CRUST

All H_2O in our reactive-transport models was assumed to originate from dehydration reactions in subducting oceanic lithosphere. The range of magnitudes of Q was estimated from combined petrological modelling of metamorphosed oceanic lithosphere (van Keken et al., 2011) with finite-element models of modern subduction-zone thermal structures (Syracuse et al., 2010) and their shear-heating-related modulation within subducting slabs (Abers et al., 2020) to estimate the H_2O-carrying capacity of oceanic crust and lithospheric mantle as a function of depth. Their 'H_2O loss' ($q'dX$) was reported in units of [$\mathrm{Tg\ Myr^{-1}\ m^{-1}}$] (i.e., mass/[time × distance]) and described the mass of hydrous-mineral-bound H_2O [Tg] expelled from a 1 m-wide, trench-parallel segment of the subducting slab over 1 Myr through a given depth range (Dataset S1). This was calculated for a series of P- and T-parameterized depth nodes as the summed differences (between adjacent nodes) of the products of $H_2O_{wt\%}$ (for a given node), subduction velocity (v), rock thickness (dz), and rock density (ρ), as summarized in Equation (A1):

$$q'dX = \sum_{i=1}^{n} \left[(H_2O_{wt\%})_{n-1} - (H_2O_{wt\%})_{n} \right] \times v \times dz \times \rho \qquad \text{(A1)}$$

To convert these H_2O loss values (Abers et al., 2020; van Keken et al., 2011) [$\mathrm{Tg\ m^{-1}\ Myr^{-1}}$] into units appropriate for reactive-transport modelling of fluid ascent through a 3-D crustal column [$\mathrm{kg\ m^{-2}}$], we first defined a subduction-zone coordinate system in which x, y, and z corresponded to trench-parallel horizontal distance, trench-normal horizontal distance, and depth (Figure 1a), respectively. Our specific interest in 'pre-arc H_2O loss' from the subducting slab implies a depth range of 40–120 km that is bracketed by the 40 km depth of the Moho in our models and the previously estimated, 120 km depth of the top of the Farallon slab beneath the Colorado Plateau (Hernández-Uribe & Palin, 2019a). Subtracting the H_2O loss at 120 km depth ($q'dX_{z=120}$) from that at 40 km depth ($q'dX_{z=40}$) for all subduction zones in their Table 3 produced the mass of H_2O expelled within this depth range ($dq'dX_{z=40\text{–}120\ \mathrm{km}}$) across a 1 m-wide slab over 1 Myr, as summarized in Equation (A2):

$$dq'dX_{z=40-120\,km} = q'dX_{z=120\,km} - q'dX_{z=40\,km} \qquad \text{(A2)}$$

This pre-arc H_2O loss rate from $z = 40$–120 km depth was then converted into an 'average pre-arc Moho potential H_2O flux' by projecting it onto the overlying, horizontal distance that corresponds to the slab dip (θ) (Dataset S1) (Syracuse et al., 2010), using Equation (A3), where $dZ = 80$ km and $dY = dZ/\tan(\theta)$:

$$Q' = \frac{dq'dX_{z=40-120\,km}}{dY} = dq'dX_{40-120\,km} \times \frac{\tan(\theta)}{dZ} \qquad \text{(A3)}$$

The average pre-arc potential Moho H_2O flux [$\mathrm{kg\ m^{-2}\ Myr^{-1}}$] describes the average mass of H_2O that moves across a 1 $\mathrm{m^2}$ horizontal Moho surface overlying the 40–120 km depth range of a subducting slab (Dataset S1). Multiplying the average potential pre-arc Moho H_2O flux by the duration over which it occurs produces the time-integrated average pre-arc potential Moho H_2O flux [$\mathrm{kg\ m^{-2}}$] that we input into the TITRATE function of *Perple_X*. This procedure presumes that all H_2O passes through the mantle wedge without metasomatizing it; although problematic for steep-dipping slabs with a thicker mantle wedge, this is less problematic (albeit with persistent issues) for shallow-dipping slabs with a thin or non-existent mantle wedge, such as the Farallon slab beneath the Colorado Plateau.

Numbered slabs in Figure 1 include (in order of increasing slab dip) 1, Northern Peru Gap; 2, Central Peru Gap; 3, Central Chile Gap; 4, Central Cascadia; 5, North Cascadia; 6, North-Central Chile; 7, Central Chile; 8, Colombia/Ecuador; 9, Peru; 10, North Honshu; 11, North Chile; 12, South-Central Chile; 13, Aegean; 14, Nankai; 15, Central Honshu; 16, South Chile; 17, Hokkaido; 18, Alaska; 19, South Lesser Antilles; 20, Calabria; 21, Ryukyu; 22, Alaska Peninsula; 23, East

Aleutians; 24, Java; 25, Bali/Lombok; 26, Izu; 27, Central Sumatra; 28, South Kurile; 29, East Banda Sea; 30, North Sumatra; 31, Sunda Strait; 32, North Lesser Antilles; 33, South Sumatra; 34, North Kurile; 35, Kamchatka; 36, New Zealand; 37, Tonga; 38, Central Aleutians; 39, Kyushu; 40, West Banda Sea; 41, West Aleut; 42, Kermadec; 43, Guatemala/El Salvador; 44, South Marianas; 45, North Philippines; 46, Costa Rica; 47, Mexico; 48, North Marianas; 49, Nicaragua; 50, Bonin; 51, South Philippines; 52, Scotia; 53, South Vanuatu; 54, New Britain; 55, Solomon; and 56, North Vanuatu.

APPENDIX B: CRUSTAL GEOTHERM CALCULATION

A one-dimensional steady-state model incorporating heat conduction with volumetric heat production (Equation (B1)) (Turcotte & Schubert, 2002) was used to estimate a 'baseline' geotherm that represents bulk-average continental crust (Dataset S2).

$$T = T_0 + q_0\left[\frac{dz_{node}}{k}\right] - A\left[\frac{(dz_{node})^2}{2k}\right] \qquad \text{(B1)}$$

Here, T_0 = temperature at the Earth's surface [°C], T = temperature at any given depth [°C], q_0 = heat flux at the Earth's surface [$\mathrm{mW\ m^{-2}}$], dz_{node} = node thickness [km], k = thermal conductivity [$\mathrm{W\ m^{-1}{}^{\circ}C^{-1}}$], and A = radiogenic-heat production [$\mathrm{\mu W\ m^{-3}}$].

This baseline crustal geotherm is based on a 40 km-thick continental crust (Rudnick & Gao, 2014), with a 12 km-thick upper crust ($z = 0$–12 km, $A = 1.6\ \mathrm{\mu W\ m^{-3}}$), an 11 km-thick middle crust ($z = 12$–23 km, $A = 1.0\ \mathrm{\mu W\ m^{-3}}$), and a 17 km-thick lower crust ($z = 23$–40 km, $A = 0.2\ \mathrm{\mu W\ m^{-3}}$) with $T_0 = 25$°C and $q_0 = 50\ \mathrm{mW\ m^{-2}}$. We assume thermal conductivities of $k = 2.7\ \mathrm{W\ m^{-1}{}^{\circ}C^{-1}}$ for the upper crust and $k = 2.6\ \mathrm{W\ m^{-1}{}^{\circ}C^{-1}}$ for the middle–lower crust (Chapman, 1986; Rudnick et al., 1998). A pseudo-linear geothermal profile was produced along depth intervals of $dz_{node} = 1$ km thickness, then regressed and linearized through the lower and middle crust to produce P–T conditions for use in petrological modelling. Depth was converted to pressure (P) by assuming (Rudnick et al., 1998) an average crustal density of $\rho = 2.8\ \mathrm{g\ cm^{-3}}$ along the entire 40 km thickness of our model crust. This baseline geotherm has a slope of ~13°C/km (~46°C $\mathrm{kbar^{-1}}$). Calculated P–T conditions between the Moho ($z = 40$ km) and the base of the upper crust ($z = 12$ km) span ~11.0 kbar and ~590°C to ~3.3 kbar and ~230°C, respectively.

APPENDIX C: PETROLOGICAL MODELLING

Petrological modelling was performed using version 6.9.1 of *Perple_X* (Connolly & Petrini, 2002) and internally consistent thermodynamic data set *hp62ver* (Holland & Powell, 2011) in the 10-component NCKFMASHTO (Na_2O–CaO–K_2O–FeO–MgO–Al_2O_3–SiO_2–H_2O–TiO_2–O_2) compositional system. MnO was excluded as a component owing to the current lack of activity–composition relations describing the partitioning behaviour of Mn^{2+} in pyroxene and amphibole, which are key components of metamorphosed basic and intermediate rocks. If included, MnO would cause significant over-stabilization of garnet beyond its natural limits. The activity–composition relations employed for modelling each lithology are given in Table 2 (Green et al., 2007, 2016; Holland & Powell, 2003, 2011; White et al., 2014).

Closed-system, 'static' petrological modelling considered the petrological changes that would occur due to instantaneous hydration of a crustal column throughout its entire depth range. Petrological changes due to instantaneous hydration were based on the differences between nominally anhydrous and minimally hydrated model lithologies along our ~13°C/km model geotherm (Section 3.2.1). The modelled crustal depth range from 40 to 12 km was discretized into 200 nodes, each of which had a thickness of $dz_{node} \approx 140$ m. Full results for closed-system, 'static' petrological models are provided in Dataset S3.

Reactive-transport modelling considered the petrological changes that would occur due to an upward-infiltrating, time-integrated basal mass flux of H_2O fluid through a one-dimensional rock column with the same ~13°C/km model geotherm that was used for closed-system models. This rock column was allowed to expand or compress and isostatically adjust according to hydration-induced changes in bulk-rock density, thus simulating surface uplift due to hydration. This was conducted using the TITRATE function of *Perple_X* (Connolly, 2005). To model mineral and bulk-rock properties for fixed H_2O-infiltration magnitudes ($Q = 0$, 0.2×10^6, and $0.8 \times 10^6\ \mathrm{kg\ m^{-2}}$), our setup discretized the modelled crustal depth range between 39.5 and 12.5 km into 100 nodes (each of which had a thickness of $dz_{node} \approx 270$ m) between the Moho (40 km depth) and the upper middle crust (12 km depth). Models of mineral H_2O content and bulk-rock density as functions of variable H_2O-infiltration magnitude (Q) were discretized into 28 nodes (each of which had a thickness of $dz_{node} = 1$ km). The initial, pre-hydration state for each node ($Q = 0$) had the same composition and fluid content as the nominally anhydrous equivalent depths used for closed-system modelling. The upper crust (0–12 km depth) was not considered here, as metamorphic reactions are not expected to proceed effectively at such shallow depths due to sluggish kinetics that characterize low-temperature environments. Post-hydration modal abundances, bulk-rock densities, and (crystallographically bound) H_2O concentrations were calculated only for solid phases, following the protocol for closed-system models. Full results for reactive-transport, open-system, 'dynamic' petrological modelling are provided in Dataset S4.

Upon entering a node from its base, the infiltrating H_2O fluid was allowed to metasomatize the pre-existing, nominally anhydrous lithology and produce a new equilibrium assemblage, as governed by H_2O infiltration magnitude (Q), bulk-rock chemistry (X), pressure (P), and temperature (T). Metasomatism thus proceeds up the crustal column and any added H_2O may either be consumed within a node, leaving a fluid-undersaturated assemblage that can further react, or pass through the node into the overlying one, where it may continue to ascend and induce reaction. The model parameter Q [kg m^{-2}] was used to specify the basal fluid-infiltration mass of H_2O fluid that vertically migrates through a horizontal 1 m^2 area. Values of Q were chosen to simulate the global variation in fluid release from subducted slabs, as discussed above.

APPENDIX D: ISOSTATIC-UPLIFT POTENTIAL

The single-node isostatic-uplift potential (δh) due to hydration in all three lithologies and hydration scenarios was calculated following equation D1 (Turcotte & Schubert, 2002), where dz_{node} is crustal-node thickness; $\rho_{c,hyd}$ is hydrated crustal density (modelled); $\rho_{c,anh}$ is nominally anhydrous crustal density (modelled); and $\rho_{c,m}$ is mantle density (3.3 g cm^{-3}):

$$\delta h = \frac{dz_{node}\left(\rho_{c,hyd} - \rho_{c,anh}\right)}{\rho_m} \tag{D1}$$

Single-node isostatic-uplift potential can be expressed as a percentage [%] normalized to node thickness ($100\% \times \delta h / dz_{node}$) to ascertain local contributions to uplift throughout the model crustal column independent of node thickness, or as absolute distance [m] to ascertain cumulative surface uplift for the full model crustal column. Following the discretization of our model crustal columns in our petrological models (Appendix C), the number of discrete, single-node isostatic-uplift potentials includes 200 nodes for closed-system models and 100 nodes for open-system models. Discrete, single-node isostatic-uplift potentials were summed upwards from the Moho to the top of the middle crust following Equation (D2) to produce cumulative surface-uplift estimates (Δh) for each lithology and hydration scenario:

$$\Delta h = \sum_{i=1}^{n} (\delta h)_n \tag{D2}$$

Our setup assumed that all metasomatism-driven displacement occurred in the vertical plane. Results are provided in Dataset S3 for static, closed-system models and in Dataset S4 for reactive-transport, open-system models.